J|A|C|S ARTICLES

Published on Web 02/16/2009

Solid-State Chlorine NMR of Group IV Transition Metal Organometallic Complexes

Aaron J. Rossini,[†] Ryan W. Mills,[†] Graham A. Briscoe,[†] Erin L. Norton,[†] Stephen J. Geier,[†] Ivan Hung,[†] Shaohui Zheng,[‡] Jochen Autschbach,*[,‡] and Robert W. Schurko*[,†]

Department of Chemistry and Biochemistry, University of Windsor, Windsor, Ontario, Canada N9B 3P4, and Department of Chemistry, The State University of New York, Buffalo, New York 14260-3000

Received October 31, 2008; E-mail: jochena@buffalo.edu; rschurko@uwindsor.ca

Abstract: Static solid-state ^{35}Cl ($I = {}^3/_2$) NMR spectra of the organometallic compounds Cp_2TiCl_2, $CpTiCl_3$, Cp_2ZrCl_2, Cp_2HfCl_2, $Cp^*_2ZrCl_2$, $CpZrCl_3$, Cp^*ZrCl_3, $Cp_2ZrMeCl$, $(Cp_2ZrCl)_2\mu$-O, and Cp_2ZrHCl (Schwartz's reagent) have been acquired at 9.4 T with the quadrupolar Carr−Purcell Meiboom−Gill (QCPMG) sequence in a piecewise manner. Spectra of several samples have also been acquired at 21.1 T. The electric field gradient (EFG) tensor parameters, the quadrupolar coupling constant (C_Q) and quadrupolar asymmetry parameter (η_Q), are readily extracted from analytical simulations of the spectra. The ^{35}Cl EFG and chemical-shift tensor parameters are demonstrated to be sensitive probes of metallocene structure and allow for differentiation of monomeric and oligomeric structures. First-principles calculations of the ^{35}Cl EFG parameters successfully reproduce the experimental values and trends. The origin of the observed values of $C_Q(^{35}Cl)$ are further examined with natural localized molecular orbital (NLMO) analyses. The combination of experimental and theoretical methods applied to the model compounds are employed to structurally characterize Schwartz's reagent (Cp_2ZrHCl), for which a crystal structure is unavailable. Aside from a few select examples of single-crystal NMR spectra, this is the first reported application of solid-state ^{35}Cl NMR spectroscopy to molecules with covalently bound chlorine atoms. It is anticipated that the methodology outlined herein will find application in the structural characterization of a wide variety of chlorine-containing transition-metal and main-group systems.

Introduction

The term "metallocene revolution" has been used to describe the increased use of transition-metal metallocene catalysts in industrial olefin polymerization processes over the last fifteen years.[1−4] Metallocene catalysts have found use as homogeneous catalysts, which are dissolved in solution and reacted with the olefin, or as heterogeneous catalysts, which are immobilized on a support material and applied in gas- or slurry-phase processes. The single-site nature of the metallocene catalysts allows for rational improvement and tuning of the polymerization performance by modification of the surface-supported organometallic species; however, this requires that "the interactions and mechanisms at work on the support surface during the immobilization, activation, and polymerization steps must be understood."[4]

Solid-state NMR (SSNMR) spectroscopy has previously been applied to examine the nature and structure of surface-supported organometallic complexes, as well as their cocatalysts, such as $AlMe_3$, methylalumoxane (MAO), and borane complexes.[5−15] The majority of these studies have utilized ^{1}H, ^{13}C, and ^{29}Si SSNMR. ^{13}C SSNMR studies have clearly demonstrated that cyclopentadienyl ligands remain bound to the metal upon immobilization on surfaces and that metal-bound alkyl ligands may be transferred to Lewis acid sites on alumina and silica supports.[6−8,12,14,15] While this information provides much insight into the catalytic processes, there are still many uncertainties regarding the exact nature of the metal−surface bond and

[†] University of Windsor.
[‡] The State University of New York, Buffalo.

(1) Soga, K. *Macromol. Symp.* **1996**, *101*, 281–288.
(2) Sinclair, K. B.; Wilson, R. B. *Chem. Ind.* **1994**, 857–862.
(3) Hlatky, G. G. *Chem. Rev.* **2000**, *100*, 1347–1376.
(4) Severn, J. R.; Chadwick, J. C.; Duchateau, R.; Friederichs, N. *Chem. Rev.* **2005**, *105*, 4073–4147.
(5) He, M. Y.; Xiong, G. X.; Toscano, P. J.; Burwell, R. L.; Marks, T. J. *J. Am. Chem. Soc.* **1985**, *107*, 641–652.
(6) Toscano, P. J.; Marks, T. J. *J. Am. Chem. Soc.* **1985**, *107*, 653–659.
(7) Toscano, P. J.; Marks, T. J. *Langmuir* **1986**, *2*, 820–823.
(8) Dahmen, K. H.; Hedden, D.; Burwell, R. L.; Marks, T. J. *Langmuir* **1988**, *4*, 1212–1214.
(9) Vasnetsov, S. A.; Nosov, A. V.; Mastikhin, V. M.; Zakharov, V. A. *J. Mol. Catal.* **1989**, *53*, 37–41.
(10) Sishta, C.; Hathorn, R. M.; Marks, T. J. *J. Am. Chem. Soc.* **1992**, *114*, 1112–1114.
(11) Reven, L. *J. Mol. Catal.* **1994**, *86*, 447–477.
(12) Ahn, H.; Marks, T. J. *J. Am. Chem. Soc.* **2002**, *124*, 7103–7110.
(13) Atiqullah, M.; Akhtar, M. N.; Faiz, M.; Moman, A.; Abu-Raqabah, A. H.; Khan, J. H.; Wazeer, M. I. *Surf. Interface Anal.* **2006**, *38*, 1319–1327.
(14) Joubert, J.; Delbecq, F.; Sautet, P.; Le Roux, E.; Taoufik, M.; Thieuleux, C.; Blanc, F.; Coperet, C.; Thivolle-Cazat, J.; Basset, J. M. *J. Am. Chem. Soc.* **2006**, *128*, 9157–9169.
(15) Jezequel, M.; Dufaud, V.; Ruiz-Garcia, M. J.; Carrillo-Hermosilla, F.; Neugebauer, U.; Niccolai, G. P.; Lefebvre, F.; Bayard, F.; Corker, J.; Fiddy, S.; Evans, J.; Broyer, J. P.; Malinge, J.; Basset, J. M. *J. Am. Chem. Soc.* **2001**, *123*, 3520–3540.

cocatalyst−metal−surface interactions. For example, immobilizing the metallocene precatalyst onto the support and subsequently activating with cocatalyst often gives different polymers than contacting the support with cocatalyst and then immobilizing the metallocene.[3]

In light of this, as well as the fact that the organometallic metal center is believed to be the active catalytic site in most cases, we have been investigating metallocene structure and dynamics from the perspective of SSNMR of quadrupolar metal nuclei, including ^{91}Zr, ^{93}Nb, and ^{139}La, in metallocene systems that are similar to or commonly used as polymerization precatalysts.[16−18] Several solution NMR studies of quadrupolar metal nuclei in transition-metal metallocenes have prefaced and inspired our studies.[19−24] We have found that the NMR spectra of these half-integer quadrupolar nuclei are responsive to both subtle and dramatic changes in molecular structure and should serve as excellent probes of metallocene chemistry in homogeneous catalysts and actual heterogeneous catalysts.

Chlorine is frequently found as a ligand in organometallic transition-metal complexes, including many of those important in catalytic polymerization processes, and may act as a useful NMR probe. There are two naturally occurring NMR-active nuclei of chlorine, ^{35}Cl and ^{37}Cl, both of which are spin $I = {}^3/_2$ nuclei that are present in high natural abundance (75.78 and 24.22%, respectively). They are considered to be low gyromagnetic ratio ("low γ") nuclei ($\nu_0 = 39.19$ and 32.62 MHz, respectively, at 9.4 T) and possess relatively small quadrupole moments ($Q = -8.165$ and -6.435 fm^2, respectively).[25] The ^{35}Cl nucleus is preferred for most NMR experiments because of its higher receptivity; however, acquisition of ^{37}Cl NMR spectra is sometimes useful, since ^{35}Cl and ^{37}Cl powder patterns are affected to different extents by anisotropic quadrupolar and chemical-shielding parameters, allowing for the measurement of chlorine chemical-shielding anisotropy (CSA).

Bryce and Sward[26] have recently presented a thorough review of SSNMR spectroscopy of quadrupolar halogen nuclei. To date, there are ∼80 publications featuring $^{35/37}$Cl SSNMR spectra. Despite the relatively favorable nuclear properties of both chlorine isotopes and the ubiquity of chlorine in many chemical systems, the application of chlorine NMR spectroscopy is usually limited to systems in which chlorine atoms reside in environments of high symmetry. The quadrupolar interaction is greatly reduced in such environments, resulting in small quadrupolar coupling constants ($C_Q = 0.1-6.0$ MHz) and correspondingly narrow, easily acquired powder patterns.[27,28] There are numerous representative examples of such systems for which ^{35}Cl SSNMR spectra have been acquired, including ionic metal chlorides,[29−31] perchlorates,[32] amino acid hydrochlorides,[33−36] and HCl pharmaceuticals.[37]

In many systems, the chlorine atoms reside in terminal or bridging environments with low spherical symmetry, and the ^{35}Cl nuclei experience correspondingly large quadrupolar interactions. In these cases, second-order quadrupolar broadening can result in powder patterns that are hundreds to thousands of kilohertz in breadth, complicating spectral acquisition with routine methods. Nuclear quadrupole resonance[38] (NQR) spectroscopy is predominantly used for the determination of larger values of $C_Q(^{35}\text{Cl})$ (i.e., ∼10 MHz and larger); however, specialized NQR experiments[39−41] must be performed in order to obtain the EFG quadrupolar asymmetry parameter (η_Q), and the chemical shift (CS) parameters are available only from ^{35}Cl NMR experiments. Single-crystal NMR spectroscopy has traditionally been the preferred method for the determination of ^{35}Cl CS and EFG parameters for systems with large $C_Q(^{35}\text{Cl})$ values; however, this method is limited because it relies on the isolation of large single crystals. For example, single-crystal ^{35}Cl NMR spectra of *p*-dichlorobenzene reveal that $C_Q = 73.96$ MHz and $\eta_Q = 0.071$,[42] corresponding to a central-transition powder pattern with a breadth of more than 10 MHz at 21.1 T. Many other systems possess chlorine nuclei with more moderate values of C_Q, for which SSNMR spectra of powdered samples may be obtained. To date, the largest value of C_Q measured by ^{35}Cl SSNMR on a powdered sample is that of aluminum trichloride ($C_Q = 9.4$ MHz),[43] which has a ^{35}Cl powder pattern with a breadth of over 250 kHz at 14.1 T. ^{35}Cl quadrupolar parameters for halogenated transition-metal metallocenes fall into this intermediate regime. For instance, ^{35}Cl NQR spectra acquired by Bryukhova and co-workers[44,45] revealed values of C_Q ranging from ∼16 MHz in $CpTiCl_3$ to 24 MHz in Cp_2TiCl_2, corresponding to ^{35}Cl SSNMR powder patterns 1−3 MHz in breadth at moderate magnetic field strengths (e.g., 9.4 T).

(16) Hamaed, H.; Lo, A. Y. H.; Lee, D. S.; Evans, W. J.; Schurko, R. W. *J. Am. Chem. Soc.* **2006**, *128*, 12638–12639.
(17) Lo, A. Y. H.; Bitterwolf, T. E.; Macdonald, C. L. B.; Schurko, R. W. *J. Phys. Chem. A* **2005**, *109*, 7073–7087.
(18) Hung, I.; Schurko, R. W. *J. Phys. Chem. B* **2004**, *108*, 9060–9069.
(19) Hao, N.; Sayer, B. G.; Denes, G.; Bickley, D. G.; Detellier, C.; McGlinchey, M. J. *J. Magn. Reson.* **1982**, *50*, 50–63.
(20) Dormond, A.; Fauconet, M.; Leblanc, J. C.; Moise, C. *Polyhedron* **1984**, *3*, 897–900.
(21) Berger, S.; Bock, W.; Marth, C. F.; Raguse, B.; Reetz, M. T. *Magn. Reson. Chem.* **1990**, *28*, 559–560.
(22) Buhl, M.; Hopp, G.; von Philipsborn, W.; Beck, S.; Prosenc, M. H.; Rief, U.; Brintzinger, H. H. *Organometallics* **1996**, *15*, 778–785.
(23) von Philipsborn, W. *Chem. Soc. Rev.* **1999**, *28*, 95–105.
(24) Pinkas, J.; Lycka, A.; Sindelar, P.; Gyepes, R.; Varga, V.; Kubista, J.; Horacek, M.; Mach, K. *J. Mol. Catal. A: Chem.* **2006**, *257*, 14–25.
(25) Harris, R. K.; Becker, E. D.; De Menezes, S. M. C.; Goodfellow, R.; Granger, P. *Pure Appl. Chem.* **2001**, *73*, 1795–1818.
(26) Bryce, D. L.; Sward, G. D. *Magn. Reson. Chem.* **2006**, *44*, 409–450.
(27) Akitt, J. W.; McDonald, W. S. *J. Magn. Reson.* **1984**, *58*, 401–412.
(28) Kentgens, A. P. M. *Geoderma* **1997**, *80*, 271–306.
(29) Bryce, D. L.; Bultz, E. B. *Chem.—Eur. J.* **2007**, *13*, 4786–4796.
(30) Kanda, T. *J. Phys. Soc. Jpn.* **1955**, *10*, 85–88.
(31) Yamagata, Y. *J. Phys. Soc. Jpn.* **1964**, *19*, 10–23.
(32) Skibsted, J.; Jakobsen, H. J. *Inorg. Chem.* **1999**, *38*, 1806–1813.
(33) Bryce, D. L.; Gee, M.; Wasylishen, R. E. *J. Phys. Chem. A* **2001**, *105*, 10413–10421.
(34) Gervais, C.; Dupree, R.; Pike, K. J.; Bonhomme, C.; Profeta, M.; Pickard, C. J.; Mauri, F. *J. Phys. Chem. A* **2005**, *109*, 6960–6969.
(35) Bryce, D. L.; Sward, G. D. *J. Phys. Chem. B* **2006**, *110*, 26461–26470.
(36) Bryce, D. L.; Sward, G. D.; Adiga, S. *J. Am. Chem. Soc.* **2006**, *128*, 2121–2134.
(37) Hamaed, H.; Pawlowski, J. M.; Cooper, B. F. T.; Fu, R.; Eichhorn, S. H.; Schurko, R. W. *J. Am. Chem. Soc.* **2008**, *130*, 11056–11065.
(38) Lucken, E. A. C. *Nuclear Quadrupole Coupling Constants*; Academic Press: London, 1969; p 360.
(39) Ramachandran, R.; Oldfield, E. *J. Chem. Phys.* **1984**, *80*, 674–677.
(40) Harbison, G. S.; Slokenbergs, A.; Barbara, T. M. *J. Chem. Phys.* **1989**, *90*, 5292–5298.
(41) Harbison, G. S.; Slokenbergs, A. *Z. Naturforsch., A: J. Phys. Sci.* **1990**, *45*, 575–580.
(42) Creel, R. B.; Von Meerwall, E.; Griffin, C. F.; Barnes, R. G. *J. Chem. Phys.* **1973**, *58*, 4930–4935.
(43) Sandland, T. O.; Du, L.-S.; Stebbins, J. F.; Webster, J. D. *Geochim. Cosmochim. Acta* **2004**, *68*, 5059–5069.
(44) Bryukhova, E. V.; Semin, G. K.; Alimov, I. M.; Nesmeyan, A. N.; Nogina, O. V.; Dubovits, V. A.; Kuznetsov, S. I. *J. Organomet. Chem.* **1974**, *81*, 195–199.
(45) Kuznetsov, S. I.; Bryukhova, E. V.; Khotsyanova, T. L.; Semin, G. K. *Z. Naturforsch., A: J. Phys. Sci.* **1994**, *49*, 627–629.

Chart 1. Organometallic Complexes for Which Solid-State ^{35}Cl NMR Spectra Have Been Acquired

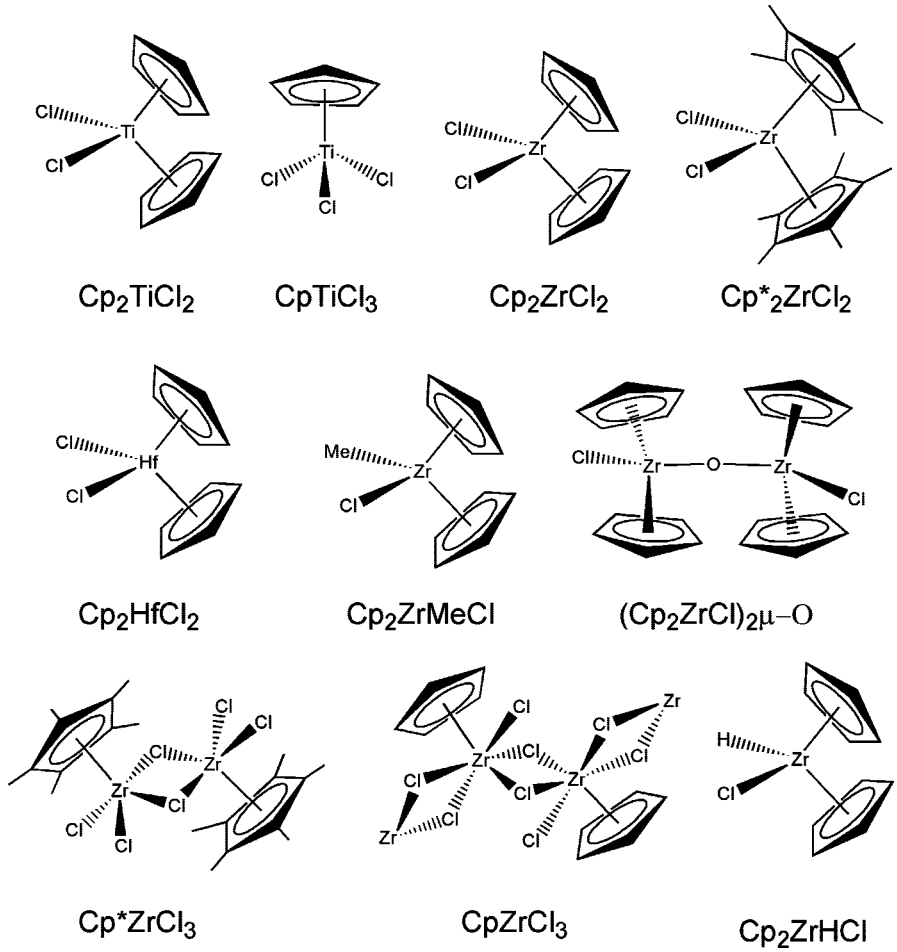

The complexes are bis(cyclopentadienyl)titanium dichloride (Cp_2TiCl_2), cyclopentadienyltitanium trichloride ($CpTiCl_3$), bis(cyclopentadienyl)zirconium dichloride (Cp_2ZrCl_2), bis(pentamethylcyclopentadienyl)zirconium dichloride ($Cp^*_2ZrCl_2$), bis(cyclopentadienyl)hafnium dichloride (Cp_2HfCl_2), methylbis-(cyclopentadienyl)zirconium chloride ($Cp_2ZrMeCl$), Oxobis[bis(cyclopentadienyl)zirconium chloride] [$(Cp_2ZrCl)_2\mu$-O], pentamethylcyclopentadienylzirconium trichloride (Cp^*ZrCl_3), cyclopentadienylzirconium trichloride ($CpZrCl_3$), and bis(cyclopentadienyl)zirconium chloride hydride (Cp_2ZrHCl, Schwartz's reagent).

The extreme breadths of such ^{35}Cl powder patterns necessitates the use of frequency-stepped NMR techniques,[46−53] where separate spin echoes are acquired at evenly spaced transmitter frequencies. The total spectrum is then formed either by plotting the echo intensities as a function of transmitter frequency[46,48,49,51] or by Fourier transforming the spin echoes and coadding/projecting the subspectra.[47,50,52,53] While this methodology is successful for acquiring broad powder patterns, the inherently low signal-to-noise ratios of broadened NMR spectra leads to long experiment times. Recently, the Carr−Purcell Meiboom−Gill (CPMG) sequence[54,55] has been reintroduced as a method for signal enhancement in NMR spectra of quadrupolar nuclei (where it is known as the QCPMG sequence).[56−60] The combination of the QCPMG pulse sequence and frequency-stepped techniques is especially useful for the rapid acquisition of extremely broad powder patterns.[16,18,50,61−63]

The current work involves three major facets. First, we demonstrate the application of ultra-wide-line QCPMG (UW-QCPMG) technique for the rapid acquisition of ^{35}Cl SSNMR

(46) Rhodes, H. E.; Wang, P. K.; Stokes, H. T.; Slichter, C. P.; Sinfelt, J. H. *Phys. Rev. B* **1982**, *26*, 3559–3568.
(47) Sparks, S. W.; Ellis, P. D. *J. Am. Chem. Soc.* **1986**, *108*, 3215–3218.
(48) Bastow, T. J. *Z. Naturforsch., A: J. Phys. Sci.* **1994**, *49*, 320–328.
(49) Bastow, T. J.; Smith, M. E. *Solid State Nucl. Magn. Reson.* **1992**, *1*, 165–174.
(50) Lipton, A. S.; Wright, T. A.; Bowman, M. K.; Reger, D. L.; Ellis, P. D. *J. Am. Chem. Soc.* **2002**, *124*, 5850–5860.
(51) Kennedy, M. A.; Vold, R. L.; Vold, R. R. *J. Magn. Reson.* **1991**, *92*, 320–331.
(52) Medek, A.; Frydman, V.; Frydman, L. *J. Phys. Chem. A* **1999**, *103*, 4830–4835.
(53) Massiot, D.; Farnan, I.; Gautier, N.; Trumeau, D.; Trokiner, A.; Coutures, J. P. *Solid State Nucl. Magn. Reson.* **1995**, *4*, 241–248.
(54) Meiboom, S.; Gill, D. *Rev. Sci. Instrum.* **1958**, *29*, 688–691.
(55) Carr, H. Y.; Purcell, E. M. *Phys. Rev.* **1954**, *94*, 630–638.
(56) Larsen, F. H.; Jakobsen, H. J.; Ellis, P. D.; Nielsen, N. C. *J. Phys. Chem. A* **1997**, *101*, 8597–8606.
(57) Cheng, J. T.; Ellis, P. D. *J. Phys. Chem.* **1989**, *93*, 2549–2555.
(58) Larsen, F. H.; Jakobsen, H. J.; Ellis, P. D.; Nielsen, N. C. *Mol. Phys.* **1998**, *95*, 1185–1195.
(59) Larsen, F. H.; Jakobsen, H. J.; Ellis, P. D.; Nielsen, N. C. *Chem. Phys. Lett.* **1998**, *292*, 467–473.
(60) Larsen, F. H.; Jakobsen, H. J.; Ellis, P. D.; Nielsen, N. C. *J. Magn. Reson.* **1998**, *131*, 144–147.
(61) Tang, J. A.; Masuda, J. D.; Boyle, T. J.; Schurko, R. W. *Chem PhysChem* **2006**, *7*, 117–131.
(62) Hung, I.; Rossini, A. J.; Schurko, R. W. *J. Phys. Chem. A* **2004**, *108*, 7112–7120.
(63) Lipton, A. S.; Bergquist, C.; Parkin, G.; Ellis, P. D. *J. Am. Chem. Soc.* **2003**, *125*, 3768–3772.

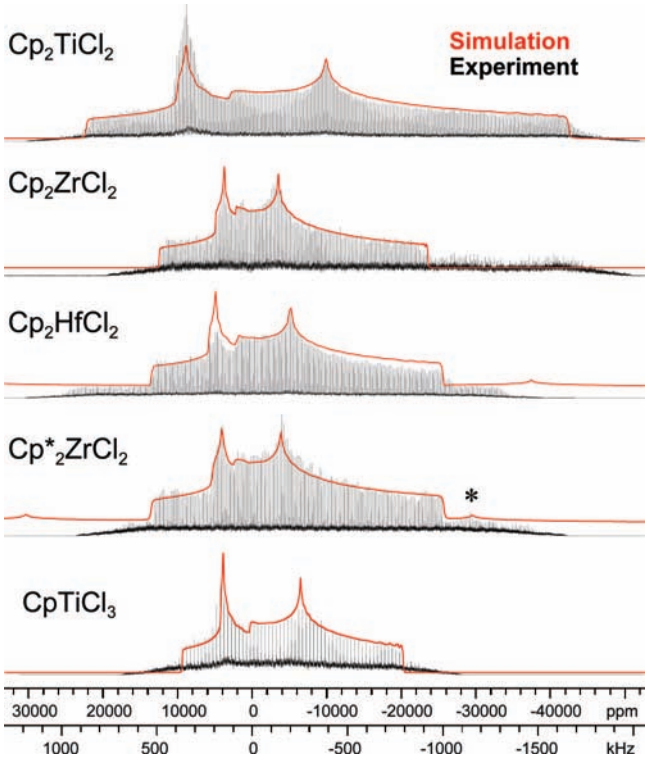

Figure 1. ^{35}Cl QCPMG SSNMR spectra and analytical simulations of the spectra (solid traces) for Cp_2TiCl_2, Cp_2ZrCl_2, Cp_2HfCl_2, $Cp^*_2ZrCl_2$, and $CpTiCl_3$. Satellite transitions are visible in the spectra of Cp_2ZrCl_2, $Cp_2{}^*ZrCl_2$, and Cp_2HfCl_2 and were included in simulations of the spectra of $Cp_2{}^*ZrCl_2$ and Cp_2HfCl_2 in order to improve the quality of the fits. The asterisk in the spectrum of $Cp^*_2ZrCl_2$ denotes a discontinuity of a satellite transition.

spectra of early-transition-metal organometallic compounds (Chart 1) at moderate (9.4 T) and high (21.1 T) magnetic fields. Second, the origin of the observed ^{35}Cl NMR parameters are examined with quantum-chemical methods, including Hartree−Fock (HF) and density functional theory (DFT). For the first time, the contributions of individual occupied MOs to the EFG tensors are analyzed within a natural localized molecular orbital (NLMO) framework. Differences in the first coordination sphere of the metal (e.g., Cp_2ZrCl_2 vs $Cp_2ZrMeCl$) and their profound impact on the observed ^{35}Cl NMR parameters are discussed in detail. Finally, application of our methodology (i.e., the combination of wide-line ^{35}Cl SSNMR and quantum-chemical calculations) is demonstrated in the characterization of an important organometallic reagent, Cp_2ZrHCl (Schwartz's reagent), whose solid-state structure is unknown at present.

Results and Discussion

Solid-State ^{35}Cl NMR Spectroscopy. Before the individual complexes are discussed, there are some common features of the ^{35}Cl SSNMR spectra that should be addressed. First, very broad powder patterns are observed for all of the complexes at 9.4 T (Figures 1−3) and 21.1 T (Figure 4), with minimum breadths of 1 MHz and 500 kHz, respectively. Second, given the breadths of the ^{35}Cl powder patterns, chemically similar (e.g., having comparable bond lengths, angles, etc.) but crystallographically distinct chlorine sites cannot be resolved in the ^{35}Cl NMR spectra. This means that the spectra essentially correspond to those of single chlorine sites and that their simulations represent average values of the NMR parameters. However, it is possible to resolve chlorine sites in different bonding

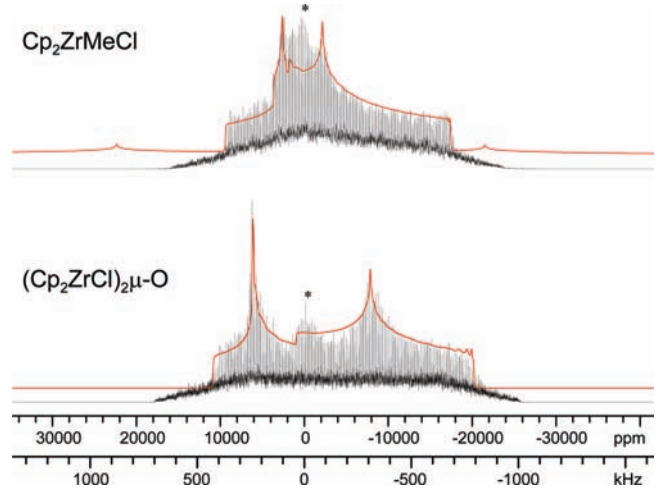

Figure 2. ^{35}Cl QCPMG SSNMR spectra and analytical simulations of the spectra (solid traces) for $Cp_2ZrMeCl$ and $(Cp_2ZrCl)_2\mu$-O. The simulation of the spectrum of $Cp_2ZrMeCl$ includes the satellite transitions. A minor impurity (marked with an asterisk), which is most likely aniline hydrochloride, is visible in the central region of each spectrum.

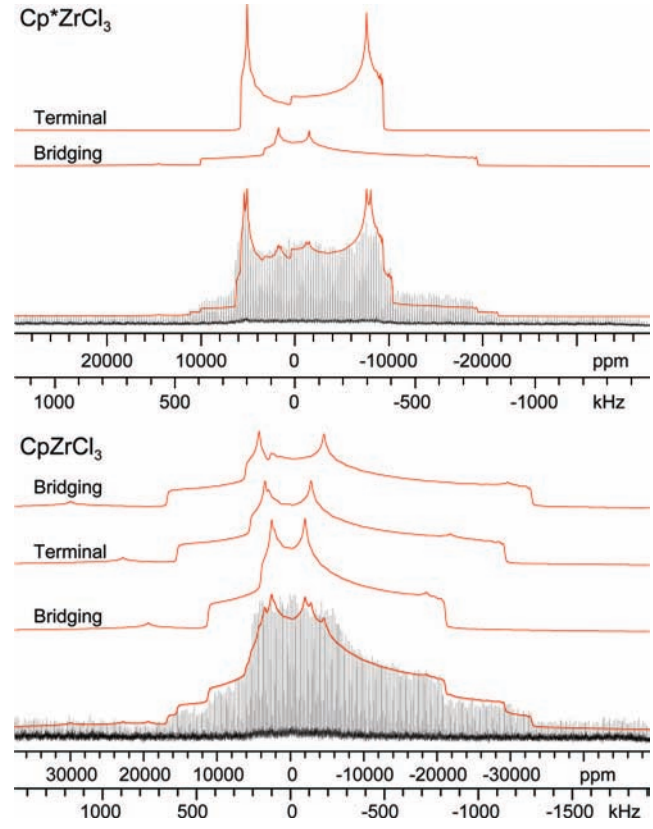

Figure 3. ^{35}Cl QCPMG SSNMR spectra and analytical simulations of the spectra (solid traces) for Cp^*ZrCl_3 and $CpZrCl_3$. Satellite transitions are visible in the spectra of both complexes. The simulation of the Cp^*ZrCl_3 spectrum utilized four sites (two bridging and two terminal); representative simulations of bridging and terminal sites are shown (see Figure S2 in the Supporting Information for all of the simulations).

environments (e.g., the bridging and terminal chlorine sites in Cp^*ZrCl_3; see below). Third, despite the large breadths of the ^{35}Cl static powder patterns, which range from ∼1.0 to 2.5 MHz at 9.4 T, the spectra can be acquired in a piecewise manner using the QCPMG pulse sequence within a reasonable time frame (e.g., 1.6−28 h). This is due to the generally long ^{35}Cl transverse relaxation time constants (T_2), which permit the

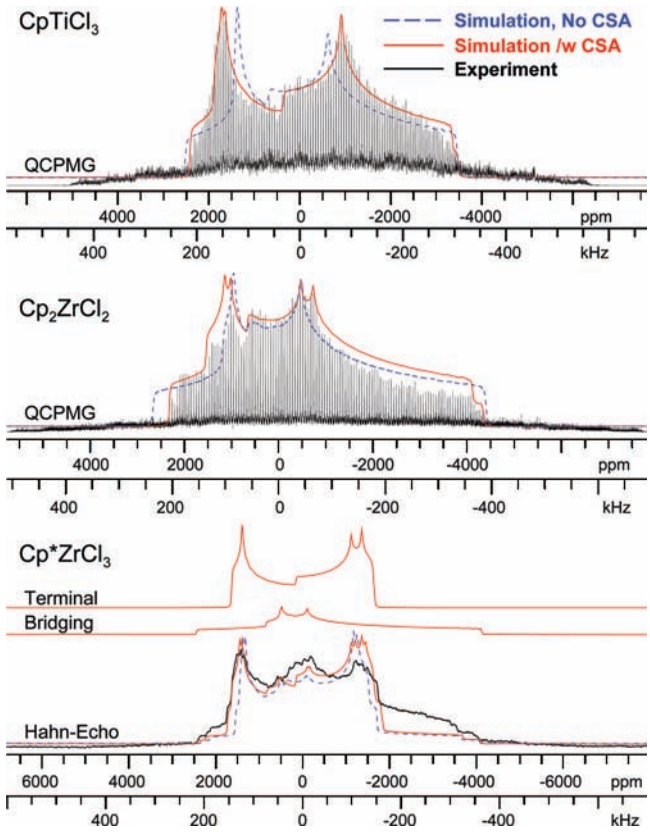

Figure 4. ^{35}Cl SSNMR spectra of $CpTiCl_3$, Cp_2ZrCl_2, and Cp^*ZrCl_3 acquired at 21.1 T and analytical simulations of the spectra with and without CSA (solid red and dashed blue traces, respectively). Piecewise QCPMG spectra were acquired for $CpTiCl_3$ and Cp_2ZrCl_2. A piecewise Hahn-echo spectrum was acquired for Cp^*ZrCl_3. Representative simulations of the bridging and terminal sites are shown for Cp^*ZrCl_3.

Table 1. Summary of Observed ^{35}Cl EFG and CS Tensor Parameters[a]

compound	C_Q (MHz)[b]	η_Q[b]	δ_{iso} (ppm)[c]
Cp_2TiCl_2	22.1(5)	0.61(3)	500(500)
Cp_2ZrCl_2	16.0(5)	0.72(4)	300(150)
Cp_2HfCl_2	17.1(4)	0.65(5)	400(500)
$Cp^*_2ZrCl_2$	16.7(4)	0.73(3)	400(400)
$CpTiCl_3$	15.5(4)	0.54(5)	500(150)
$Cp_2ZrMeCl$	13.7(4)	0.75(10)	400(400)
$(Cp_2ZrCl)_2\mu$-O	16.3(4)	0.43(7)	300(400)
Cp^*ZrCl_3 [site 1]	12.8(5)	0.10(10)	400(200)
Cp^*ZrCl_3 [site 2]	13.3(5)	0.12(10)	400(200)
Cp^*ZrCl_3 [site 3]	14.6(5)	0.88(10)	200(200)
Cp^*ZrCl_3 [site 4]	14.0(5)	0.80(10)	200(200)
$CpZrCl_3$ [multiple sites][d]	14.8−18.6	0.7−0.8	300
Cp_2ZrHCl	19.7(3)	0.20(4)	80(50)

[a] The uncertainty in the last digit(s) of each value is denoted in brackets. [b] The EFG tensor is described by three principal components V_{jj} (j = 1−3) ordered such that $|V_{11}| \le |V_{22}| \le |V_{33}|$. In terms of these components, $C_Q = eQV_{33}/h$ and $\eta_Q = (V_{11} - V_{22})/V_{33}$. [c] The CS tensor is described by three principal components δ_{jj} (j = 1−3) ordered such that $\delta_{11} \ge \delta_{22} \ge \delta_{33}$. In terms of these components, $\delta_{iso} = (\delta_{11} + \delta_{22} + \delta_{33})/3$. [d] Details are given in the text.

acquisition of long echo trains. Finally, once the total patterns have been formed by coaddition of the subspectra, analytical simulations provide values of the EFG parameters C_Q and η_Q and the isotropic chemical shift δ_{iso} (Table 1). The effects of chlorine CSA are negligible at 9.4 T (Figure S1 in the Supporting Information) but can be detected at 21.1 T, yielding the span (Ω) and skew (κ) of the CS tensor. The positions of the discontinuities are crucial for accurately determining the quadrupolar parameters, which dominate the broad second-order central transitions, while the chemical shielding parameters are somewhat less influential. Variations in intensity across these patterns can arise from a variety of sources, including small CSA contributions, interference from satellite transitions, overlap of resonances from similar but magnetically distinct chlorine sites, heteronuclear dipolar interactions, and so forth.

Cp_2MCl_2 Series. All of the group IV Cp_2MCl_2 (M = Ti, Zr, Hf) single-crystal X-ray structures contain two distinct molecules in the asymmetric unit, with four crystallographically and magnetically distinct chlorine sites.[64−66] The M−Cl distances and Cl−M−X angles are similar for all of the chlorine sites, resulting in powder patterns that essentially correspond to that of a single site for each complex. Quantum-chemical calculations (see below) and NQR spectra acquired by Bryukhova and coworkers[45] confirm this for the Cp_2MCl_2 series.

The ^{35}Cl SSNMR spectrum of Cp_2TiCl_2 consists of a second-order powder pattern that is ~2.5 MHz wide (Figure 1). Several distinct discontinuities are visible in the experimental spectrum, and all are readily reproduced by the analytical simulation, yielding $C_Q = 22.1$ MHz, $\eta_Q = 0.61$, and $\delta_{iso} = 500$ ppm (Table 1). Given the magnitude of the quadrupolar interaction, the error in the measured value of δ_{iso} is large at 9.4 T.

The ^{35}Cl SSNMR spectrum of Cp_2ZrCl_2 is best simulated with $C_Q = 16.0$ MHz, $\eta_Q = 0.72$, and $\delta_{iso} = 300$ ppm. ^{35}Cl and ^{91}Zr satellite transitions are visible at the low-frequency end (right side) of the powder pattern. The spectrum of Cp_2HfCl_2 is simulated with $C_Q = 17.1$ MHz, $\eta_Q = 0.65$, and $\delta_{iso} = 400$ ppm. The breadth of the ^{35}Cl powder patterns of Cp_2ZrCl_2 and Cp_2HfCl_2 (~1.6 MHz) are drastically reduced compared with that of Cp_2TiCl_2. The total spectrum of Cp_2ZrCl_2 was acquired in 1.6 h at 9.4 T because of the combination of a favorable T_2 and a relatively narrow powder pattern width.

Within the Cp_2MCl_2 series, there are several trends evident in the ^{35}Cl NMR parameters. The values of C_Q observed for Cp_2ZrCl_2 and Cp_2HfCl_2 are much smaller than that observed for Cp_2TiCl_2. The increased average M−Cl bond lengths in Cp_2ZrCl_2 (2.45 Å)[64] and Cp_2HfCl_2 (2.42 Å)[65] compared with the average Ti−Cl bond length in Cp_2TiCl_2 (2.37 Å) are expected to lead to reductions in the largest component of the EFG tensor, V_{33}; however, the deformation of core and valence atomic orbitals by covalent bonding interactions must also be considered.[38] Relationships between M−Cl bonding and V_{33} are addressed in Quantum-Chemical Calculations, below.

The value of C_Q for Cp_2TiCl_2 is the largest observed for this series of complexes and corresponds to a regime where the quadrupolar interaction approaches the magnitude of the Zeeman interaction. However, the analytical simulations produced by the WSolids computer program are based on the high-field approximation, where the Larmor frequency (ν_0) is assumed to be an order of magnitude larger than the quadrupolar frequency (ν_Q), allowing the latter to be treated as a perturbation on the former. Of course, this raises questions about the validity of the simulations. Fortunately, ν_Q has been measured for this

(64) Repo, T.; Klinga, M.; Mutikainen, I.; Su, Y.; Leskela, M.; Polamo, M. *Acta Chem. Scand.* **1996**, *50*, 1116–1120.
(65) Soloveichik, G. L.; Arkhireeva, T. M.; Bel'skii, V. K.; Bulychev, B. M. *Metalloorg. Khim.* **1988**, *1*, 226–230.
(66) Nieger, M.; Hupfer, H. Private communication, 1999; CSD code CDCPTI04.

Table 2. Values of C_Q Calculated from ^{35}Cl NQR Data

compound	ν_Q range (MHz)[a]	average ν_Q (MHz)[a]	C_Q (MHz) average NQR[b]	C_Q (MHz) NMR
Cp_2TiCl_2	11.787−12.090	11.91	22.46	22.1(5)
$CpTiCl_3$	7.970 and 7.984	7.97	15.28	15.5(4)
Cp_2ZrCl_2	8.558−8.756	8.68	16.04	16.0(5)
Cp_2MoCl_2	16.875−17.273	17.13	32.92	−
Cp_2WCl_2	17.723−18.063	17.84	34.28	−

[a] Taken from refs 44 and 45. The NQR measurements for Cp_2TiCl_2, Cp_2ZrCl_2, and $CpTiCl_3$ were conducted at 293.5 K. An average of the values of ν_Q for crystallographically distinct sites was used to calculate the NQR C_Q value. [b] Calculated using eq 1 with values of ν_Q taken from NQR experiments and values of η_Q from NMR experiments.

complex and others via NQR spectroscopy.[44,45] The value of ν_Q is related to the C_Q value for an $I = {}^3/_2$ nucleus by the expression

$$C_Q = \frac{2\nu_Q}{\sqrt{1 + \frac{\eta_Q^2}{3}}} \quad (1)$$

In all cases, the experimentally determined values of C_Q are within experimental error of the values predicted from NQR spectra (Table 2).[67]

$Cp^*_2ZrCl_2$. Analytical simulation of the ^{35}Cl SSNMR spectrum of $Cp_2^*ZrCl_2$ yields $C_Q = 16.7$ MHz, $\eta_Q = 0.73$, and $\delta_{iso} = 400$ ppm. The fit of the spectrum was aided by the detection of a discontinuity in the satellite transition on the low-frequency side of the powder pattern. The single-crystal X-ray structure reveals Zr−Cl bond lengths (2.46 Å) similar to those of Cp_2ZrCl_2, and correspondingly similar ^{35}Cl NMR parameters are observed.[68] There is a slight difference in the values of C_Q, suggesting that ^{35}Cl NMR spectroscopy may be able to detect differences in the Cp ligand framework.

$CpTiCl_3$. Simulation of the ^{35}Cl NMR spectra of $CpTiCl_3$ (Figure 1) yields $C_Q = 15.5$ MHz, $\eta_Q = 0.54$, and $\delta_{iso} = 500$ ppm. The values of C_Q and η_Q are significantly different from those obtained for Cp_2TiCl_2, demonstrating the sensitivity of the ^{35}Cl NMR parameters to differences in the first coordination sphere of the metal. It should also be recognized that the signal-to-noise ratio of the ^{35}Cl NMR spectrum of $CpTiCl_3$ is much lower than that of Cp_2TiCl_2 because of a much shorter T_2 in the former, which results in a shorter echo train and the acquisition of fewer echoes.

The previously reported ^{35}Cl NQR spectra of $CpTiCl_3$ display two distinct quadrupolar frequencies;[44] this result is inconsistent with the single-crystal X-ray structure reported by Engelhardt et al.,[69] which identifies three magnetically and crystallographically distinct chlorine sites. We report a newly refined structure (see Table S1 and the CIF file in the Supporting Information) that possesses two distinct Cl sites, in agreement with the NQR data. The new single-crystal X-ray structure reveals an average Ti−Cl bond length (2.22 Å) that is 0.15 Å shorter than that observed for Cp_2TiCl_2 (2.37 Å).

In a purely electrostatic (ionic) model, shorter Ti−Cl bond lengths would lead to larger C_Q values, since C_Q is proportional to V_{33}, which in turn is inversely proportional to the cube of the interatomic distance(s) (i.e., proportional to $1/r^3$) under the point-charge approximation.[38] However, the value of C_Q observed for $CpTiCl_3$ is significantly smaller than that for Cp_2TiCl_2. The difference between values of C_Q in these two species must therefore arise from differences in Ti−Cl covalent bonding. In this light, Bryukhova and co-workers[44,45] have previously ascribed the smaller C_Q in $CpTiCl_3$ to increased Ti−Cl π bonding in comparison with that in Cp_2TiCl_2. This hypothesis is further discussed in Quantum-Chemical Calculations.

$Cp_2ZrMeCl$. It has been proposed that the alkylation of an organometallic complex by an activator or cocatalyst increases the activity of surface-supported organometallic species.[3,4] Solid-state ^{35}Cl NMR spectroscopy may be useful for observing the abstraction of chloride ligands by cocatalysts and quantifying the amounts of chlorinated metallocene centers remaining after activation. Analytical simulations reveal that for $Cp_2ZrMeCl$, $C_Q = 13.7$ MHz, $\eta_Q = 0.75$, and $\delta_{iso} = 400$ ppm (Figure 2). This complex possesses the smallest value of C_Q observed in this series of complexes. It is likely that $Cp_2ZrMeCl$ has a smaller C_Q value than Cp_2ZrCl_2 because of changes in the Zr−Cl bond lengths induced by the presence of the methyl ligand (the bond lengths are 2.49 and 2.45 Å, respectively).[70] It should be noted that a minor impurity is visible, resulting in a relatively poor fit of the central part of the pattern. This impurity signal is most likely due to a small amount of aniline hydrochloride that was formed in the synthesis of the compound.

$(Cp_2ZrCl)_2\mu$-O. The oxo-bridged complex $(Cp_2ZrCl)_2\mu$-O is a synthetic precursor to $Cp_2ZrMeCl$ and is believed to be the product of the hydrolysis of $Cp_2ZrMeCl$.[71] The ^{35}Cl NMR parameters obtained from the spectrum are $C_Q = 16.3$ MHz, $\eta_Q = 0.43$, and $\delta_{iso} = 300$ ppm. This observed value of η_Q is significantly smaller than those observed for the other zirconium complexes. A minor amount of an impurity is visible in the spectrum (see above).

Cp^*ZrCl_3. Cp^*ZrCl_3 is a dimer with three magnetically distinct chlorine sites in its crystal structure.[72] Two of the chlorine atoms are terminally bound to Zr, and the third site bridges adjacent Zr centers. The spectrum of Cp^*ZrCl_3 is distinct from of those of the previous complexes (Figure 3). Specifically, the central discontinuities of the powder pattern are not readily observable, and "shoulders" are apparent at the edges of the spectrum. Because the observed powder pattern corresponds to both bridging and terminal chlorine sites, an accurate simulation of the experimental spectrum was more difficult to obtain, and larger uncertainties are associated with the NMR parameters. The general features of the spectrum can be reproduced by a simple simulation that employs large- and small-η_Q powder patterns in a 1:2 intensity ratio, the two of which possess similar values of C_Q (Figure S2 in the Supporting Information). However, in order to properly account for the shoulders, a four-site simulation must be used (two bridging and two terminal sites with 1:2 intensity ratios). The inclusion of an additional bridging site (with an η_Q value near 1) disagrees with the current crystal structure, but it is required to reproduce the shoulder features of the spectrum. The ratio of intensities suggests that the small-η_Q pattern corresponds to the terminal chloride ligands,

(67) Kuznetsov, S. I.; Bryukhova, E. V.; Semin, G. K. *Izv. Akad. Nauk SSSR, Ser. Fiz.* **1981**, *45*, 476–486.
(68) Bohme, U.; Rittmeister, B. Private communication, 1998; CSD code GEJPEQ.
(69) Engelhardt, L. M.; Papasergio, R. I.; Raston, C. L.; White, A. H. *Organometallics* **1984**, *3*, 18–20.
(70) Hunter, W. E.; Hrncir, D. C.; Bynum, R. V.; Penttila, R. A.; Atwood, J. L. *Organometallics* **1983**, *2*, 750–755.
(71) Wailes, P. C.; Weigold, H.; Bell, A. P. *J. Organomet. Chem.* **1971**, *33*, 181–188.
(72) Martin, A.; Mena, M.; Palacios, F. *J. Organomet. Chem.* **1994**, *480*, C10–C11.

Table 3. Observed ^{35}Cl CS Tensor Parameters and Euler Angles

compound	δ_{iso} (ppm)[a]	Ω (ppm)[b]	κ[c]	Euler angles (deg)[d]		
				α	β	γ
$CpTiCl_3$	500(150)	750(400)	−0.4(5)	80(30)	5(15)	5(30)
Cp_2ZrCl_2	300(150)	800(500)	0.0(5)	2(10)	72(20)	−70(20)
Cp^*ZrCl_3 [sites 1 and 2]	400(200)	500(400)	0.4(8)	10(90)	15(30)	0(90)
Cp^*ZrCl_3 [sites 3 and 4]	200(200)	200(200)	−[e]	−[e]	−[e]	−[e]

[a] Defined in footnote [c] of Table 1. [b] $\Omega = \delta_{11} - \delta_{33}$. [c] $\kappa = 3(\delta_{22} - \delta_{iso})/\Omega$. [d] The Rose convention is used for the Euler angles. [e] Overlap of sites and the small CSA make it difficult to estimate κ and the Euler angles for the bridging sites.

and quantum-chemical calculations confirm this (see below). The NMR parameters obtained for both Cp^*ZrCl_3 and $(Cp_2ZrCl)_2\mu$-O suggest that the observation of smaller values of η_Q may be used to identify the terminal chloride ligands of dimers (this information is absent from standard NQR experiments). It is also interesting to note the extremely large values of η_Q observed for the bridging ligands of the complex.

$CpZrCl_3$. $CpZrCl_3$ is a coordination polymer in the solid state.[69] The crystal structure reveals three magnetically distinct chlorine sites, with bridging and terminal chloride ligands present in a 2:1 ratio. The ^{35}Cl NMR spectrum is relatively broad and lacks central discontinuities; however, several shoulders are visible at the sides of the spectrum (Figure 3). The number of magnetically distinct sites and the lack of features make it difficult, if not impossible, to determine the NMR parameters of the individual sites. However, the appearance of the spectrum is clearly distinct from those of the complexes that possess only terminal chlorine ligands, and despite its complexity, it can be utilized to differentiate between monomeric and oligomeric metallocene species. Quantum-chemical calculations of ^{35}Cl EFG tensors (see below) can be used to provide parameter values that adequately reproduce the experimental spectrum, though there is some disagreement in the positions of the discontinuities in the experimental and simulated spectra.

Solid-State ^{35}Cl NMR Spectra Acquired at 21.1 T. It was expected that the use of high magnetic fields would be very beneficial for ^{35}Cl NMR for two reasons: first, the signal-to-noise ratio of an NMR experiment is proportional to the square of the magnetic field (B_0^2), greatly reducing the time required to acquire each subspectrum, and second, the breadths of the ^{35}Cl powder patterns are inversely proportional to B_0, greatly reducing the number of subspectra that must be acquired. The ^{35}Cl SSNMR spectra of $CpTiCl_3$, Cp_2ZrCl_2, and Cp^*ZrCl_3 at 21.1 T are shown in Figure 4. The QCPMG spectra of $CpTiCl_3$ and Cp_2ZrCl_2 were acquired in 13 and 7 min, respectively, at 21.1 T, as compared with 11 and 1.6 h, respectively, at 9.4 T.

The breadths of the ^{35}Cl powder patterns acquired at 21.1 T are reduced to approximately half of the breadths of the corresponding spectra acquired at 9.4 T, consistent with powder patterns dominated by the second-order quadrupolar interaction. However, if the spectra are simulated without accounting for chlorine CSA, relatively poor fits are obtained (dashed traces in Figure 4). Simulations of the spectra from 21.1 T that include the CS tensor parameters Ω and κ and the Euler angles α, β, and γ, which describe the relative orientations of the CS and EFG tensors[73] (Table 3), result in improved fits of the experimental spectra of $CpTiCl_3$, Cp_2ZrCl_2, and Cp^*ZrCl_3 (solid traces in Figure 4). The reader is cautioned that the errors associated with Ω, κ, and the Euler angles are large in all cases because of the relative magnitudes of the quadrupolar and chemical-shielding interactions. As a result of the overlap of multiple distinct chlorine sites in Cp^*ZrCl_3, the uncertainties associated with the CS tensor parameters and Euler angles are especially large. In general, the observed values of Ω are several times larger than those observed for amino acid hydrochlorides (Ω < 150 ppm) and alkaline-earth chlorides (Ω < 75 ppm);[29,35,36] however, given the low local symmetry about the chlorine nuclei in the organometallic complexes, the larger values of Ω are expected and are predicted by quantum-chemical calculations. Finally, simulations of the spectra at 9.4 T are seen to be largely unaffected by the inclusion of CSA (Figure S1 in the Supporting Information).

Quantum-Chemical Calculations. First-principles calculations of ^{35}Cl NMR parameters are extremely useful, as they may provide insight into the origin of the observed NMR parameters and/or aid in the interpretation of ^{35}Cl NMR data from systems that are not amenable to X-ray diffraction techniques. The origin of the observed ^{35}Cl C_Q values are further investigated within the framework of an NLMO analysis. Computations were performed with the Gaussian 03[74] and ADF[75−77] codes.

Calculations of Chlorine NMR Parameters. Chlorine basis sets for the accurate calculation of $^{35/37}$Cl EFG and CS tensor parameters have previously been suggested by Bryce et al.[36] Both B3LYP and RHF calculations employing the cc-pVDZ, cc-pVDZ DK, or aug-cc-pVDZ chlorine basis set yield EFG tensor parameters that are in excellent agreement with the experimental values (Table 4 and Table S2 in the Supporting Information). There are several notable trends in the calculated values that should be discussed. Calculations employing the RHF method and aug-cc-pVDZ basis set on chlorine consistently yield values of C_Q that are within ±5% of the experimental values for all of the monomeric complexes except for $Cp_2ZrMeCl$; however, the theoretical values of η_Q and δ_{iso} are typically smaller than the experimental values. On the other hand, B3LYP calculations generally produce more accurate values of δ_{iso} while overestimating the values of C_Q, η_Q, and Ω.

Theoretically calculated ^{35}Cl EFG tensors are distinct for terminal and bridging chlorine sites, helping to account for their disparate EFG parameters. For instance, in the dimeric Cp^*ZrCl_3 species, the theoretical values of C_Q for the bridging and terminal chlorine sites are similar in magnitude; however, for the terminal chlorine, the sign of C_Q is negative and η_Q is predicted to be near 0 (i.e., V_{33} is the unique component of the EFG tensor), whereas for the bridging chlorine, the sign of C_Q is positive and η_Q is near 1 (V_{11} is the unique component).

Calculations on $CpZrCl_3$ are complicated because it exists as a coordination polymer in the solid state. A cluster with a charge of 2− and containing three zirconium centers, three Cp rings, and nine chlorine atoms was used for calculations on $CpZrCl_3$ (Figure 5). The five chlorine atoms bound to the central Zr unit provide an adequate model of the chlorine atoms in the

(73) Power, W. P.; Wasylishen, R. E.; Mooibroek, S.; Pettitt, B. A.; Danchura, W. *J. Phys. Chem.* **1990**, *94*, 591–598.

(74) Frisch, M. J.; et al. *Gaussian 03*, rev. B.03; Gaussian, Inc.: Pittsburgh, PA, 2003.

(75) Baerends, E. J.; et al. *ADF2007*; Scientific Computing & Modelling NV: Amsterdam, 2007.

(76) Fonseca Guerra, C.; Snijders, J. G.; te Velde, G.; Baerends, E. J. *Theor. Chem. Acc.* **1998**, *99*, 391–403.

(77) te Velde, G.; Bickelhaupt, F. M.; Baerends, E. J.; Fonseca Guerra, C.; Van Gisbergen, S. J. A.; Snijders, J. G.; Ziegler, T. *J. Comput. Chem.* **2001**, *22*, 931–967.

Table 4. ^{35}Cl NMR Parameters Calculated Using the RHF Method and aug-cc-PVDZ Basis Set[a]

compound	method/Cl basis set[b]	site	C_Q (MHz)[c]	η_Q	δ_{iso} (ppm)[d]	Ω (ppm)[e,f]	κ[e,g]
Cp_2TiCl_2	experimental	−	22.1	0.62	500		
	RHF/aug-cc-pVDZ	1	−23.0	0.46	216	958	0.0
	RHF/aug-cc-pVDZ	2	−23.3	0.46	210	958	0.1
$CpTiCl_3$	experimental	−	15.5	0.54	500	750	−0.4
	RHF/aug-cc-pVDZ	1	−15.6	0.45	470	909	−0.2
	RHF/aug-cc-pVDZ	2	−15.5	0.44	478	902	−0.2
	RHF/aug-cc-pVDZ	3	−15.5	0.45	474	901	−0.3
Cp_2ZrCl_2	experimental	−	16.0	0.72	300	800	0.0
	RHF/aug-cc-pVDZ	1	−16.4	0.58	158	740	0.1
	RHF/aug-cc-pVDZ	2	−15.9	0.59	173	733	0.0
$Cp^*_2ZrCl_2$	experimental	−	16.7	0.73	400		
	RHF/aug-cc-pVDZ	1	−16.1	0.46	204	571	−0.5
Cp_2HfCl_2	experimental	−	17.1	0.65	400		
	RHF/aug-cc-pVDZ	1	−17.3	0.56	131	608	0.2
	RHF/aug-cc-pVDZ	2	−17.1	0.56	145	613	0.1
$Cp_2ZrMeCl$	experimental	−	13.7	0.75	400		
	RHF/aug-cc-pVDZ	1	−15.3	0.66	168	775	−0.1
$(Cp_2ZrCl)_2\mu$-O	experimental	−	16.3	0.43	300		
	RHF/aug-cc-pVDZ	1	−15.9	0.45	72	545	0.2
	RHF/aug-cc-pVDZ	2	−15.4	0.40	65	454	0.2
Cp^*ZrCl_3	experimental	1	12.8	0.10	400	500	0.4
	experimental	2	13.3	0.12	400	500	0.4
	experimental	3	14.6	0.88	200	200	0.0
	experimental	4	14.0	0.80	200	200	0.0
	RHF/aug-cc-pVDZ	1	−13.1	0.06	320	472	−0.2
	RHF/aug-cc-pVDZ	2	−12.0	0.07	335	478	−0.1
	RHF/aug-cc-pVDZ	3, 4	12.1	0.95	131	40	−0.4
$CpZrCl_3$	experimental	1, 2	14.8	0.80	400		
	experimental	3, 4	18.6	0.75	150		
	experimental	5	17.4	0.80	500		
	RHF/aug-cc-pVDZ	1	−15.7	0.75	257	528	−0.3
	RHF/aug-cc-pVDZ	2	−14.7	0.89	192	386	−0.2
	RHF/aug-cc-pVDZ	3	19.8	0.72	77	178	−0.6
	RHF/aug-cc-pVDZ	4	18.7	0.72	77	160	−0.4
	RHF/aug-cc-pVDZ	5	−17.4	0.72	341	688	−0.8

[a] All of the computational results can be found in Table S2 in the Supporting Information. [b] See the Theoretical Section for details concerning the basis sets used on other atoms. [c] Only the magnitude of C_Q can be measured experimentally. For definitions of the NMR parameters, refer to footnotes [b] and [c] of Table 1. [d] Theoretical values of δ_{iso} were determined by comparison to the shielding values of HCl calculated with the corresponding method and basis set (Table S2). The equation used was $\delta_{iso} = \sigma_{iso}(HCl) - \sigma_{iso} + 28$ ppm. [e] Experimental CSA parameters are available only for compounds for which a spectrum at 21.1 T was recorded. [f] Defined in footnote [b] of Table 3. [g] Defined in footnote [c] of Table 3.

full coordination polymer structure. However, there is one key difference between the cluster model and the crystal structure: the cluster contains five magnetically distinct chlorine sites, while the crystal structure contains only three distinct chlorine sites. For this reason, the NMR parameters calculated for the pairs of bridging sites were averaged to obtain the values used for the analytical simulation. The resulting analytical simulation adequately reproduces the features of the experimental spectrum (Figure 3 and Table 4), particularly the "shoulders" that are visible at the sides of the spectrum.

There are also some interesting features of the calculated NMR parameters for this complex. The two pairs of bridging chloride ligands possess significantly different calculated EFG and CS tensor parameters (see Table 4). Most notably, for one pair (sites 1 and 2), the values of C_Q are negative (−15.7 and −14.7 MHz, respectively), while for the other pair (sites 3 and 4), the values of C_Q are positive and slightly larger in magnitude (19.8 and 18.7 MHz, respectively). The EFG and CS tensor parameters for sites 1 and 2 are similar to those for the terminal chlorine sites observed in other complexes. The single-crystal

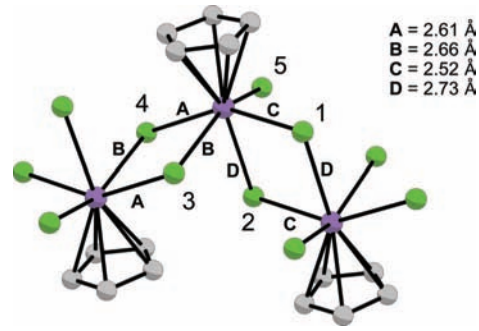

Figure 5. The cluster model used for Gaussian 03 calculations on $CpZrCl_3$. The chlorine sites in Table 4 of the manuscript are labeled. Selected bond lengths are also shown. Sites 1 and 2 are symmetry-related and magnetically distinct in this model but not in the crystal structure. Sites 3 and 4 are also magnetically distinct in the cluster model but not in the crystal structure. Therefore, averages of the calculated NMR parameters from the pairs of sites were used in the analytical simulation of the spectrum.

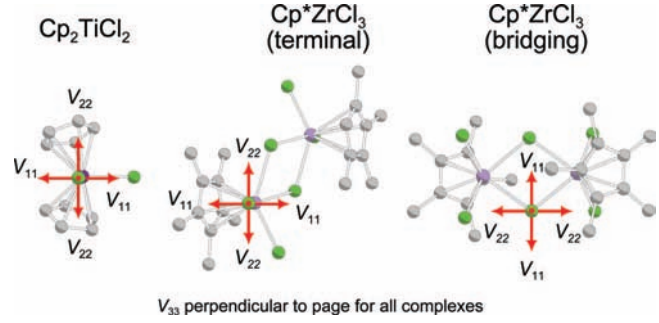

Figure 6. EFG tensor orientations in Cp_2TiCl_2 and Cp^*ZrCl_3. For Cp^*ZrCl_3, the tensor orientations are shown for both the terminal and bridging Cl sites. The orientations were taken from the calculations listed in Table 4.

X-ray structure[69] reveals that the site 1 and 2 chloride ligands are opposite Cp rings and that each makes a short (2.52 Å) and a long (2.73 Å) contact with the zirconium centers that they bridge. It would appear that the presence of a distant second zirconium center has little effect on the ^{35}Cl NMR parameters, making the NMR parameters of sites 1 and 2 more similar to those observed for terminal chloride ligands. Conversely, the geometry of sites 3 and 4 is similar to that of the bridging site observed in Cp^*ZrCl_3, with relatively equal contacts to the two zirconium centers (2.66 and 2.61 Å). This explains the similarity of the calculated NMR parameters of sites 3 and 4 of $CpZrCl_3$ to those for the bridging site of Cp^*ZrCl_3.

Visualization of the calculated orientations of the EFG tensors within molecular frames can provide insight into the origin of the observed EFG tensor parameters. Several chlorine EFG tensor orientations are shown in Figure 6. The EFG tensor orientation of Cp_2TiCl_2 is representative of terminal chlorine sites. The largest component of the EFG, V_{33}, is close to the Ti−Cl bond (with a V_{33}−Cl−Ti angle of 4.3°). Since V_{33} is directed near the metal−Cl bond in Cp_2TiCl_2, the observation that longer M−Cl bonds lead to smaller C_Q values in the Cp_2MCl_2 series is to be expected. The chlorine EFG tensor orientations for Cp^*ZrCl_3, which possesses both bridging and terminal chloride ligands, are also pictured in Figure 6. The EFG orientation of the terminal site is similar to that of Cp_2TiCl_2 (the V_{33}−Cl−Zr angle is 6.1°). Conversely, for the bridging site, V_{33} is directed perpendicular to the Zr−Cl−Zr plane (making an angle of 86° with respect to this plane). Similar V_{33} orientations were calculated for aluminum EFGs, where V_{33} is oriented perpendicular to the horizontal mirror plane of trigonal

planar systems.[61] Cartesian coordinates of the EFG tensor orientations are provided in Table S3 in the Supporting Information.

NLMO Analysis of EFG Tensors. In order to further probe the origins of the observed ^{35}Cl EFG tensor parameters, we undertook an NLMO analysis,[111–113] i.e., we determined the contributions of individual NLMOs to the observed ^{35}Cl EFGs. Computations were performed with a developer's version of the ADF code, version 2007.[75–77] For the present work, a new module was developed for an MO-based analysis of EFG tensors using either delocalized or localized MOs. A similar relativistic approach for the analysis of NMR spin−spin coupling constants and chemical shifts has been reported recently.[78–81] The full details of the NLMO EFG analysis program will be detailed in a future publication; however, a brief, detailed explanation of the analysis is given below and in Theoretical Methods.

The analysis proceeded as follows: computation of the Cartesian EFG tensors, transformation to the principal coordinate axis, transformation of the integrand in eq (7) to the principal axis, and subsequent analysis per NLMO. Quadrupole coupling constants were obtained from the relation $C_Q = eQV_{33}/h$, so the NLMO contributions to V_{33} are directly related to C_Q. In the analysis, contributions smaller than a threshold of 5% of V_{33} were omitted to keep the amount of data at a manageable level.

The information available from the NLMO analysis is similar to that from an NBO analysis[78–81,111–113] and includes classification of the NLMOs (e.g., as bonding, core, and lone-pair orbitals), the composition of the NLMOs in terms of atomic orbitals (AOs), and a measure of how well the electronic structure is described by a given Lewis structure (as indicated by occupancy numbers). NLMO EFG analyses for Cp_2TiCl_2, $CpTiCl_3$, and Cp_2ZrCl_2 were examined and compared in order to understand the origins of the chlorine EFG tensors in terms of localized MOs, for which individual, intuitive bonding, lone-pair, and core contributions to the EFG can be obtained. The generally delocalized, canonical MOs available from standard HF and DFT calculations are not as convenient for such an analysis, since many of these MOs may contribute to a local bonding environment with sometimes large contributions of opposite signs.

The output from the NLMO EFG analysis of Cp_2TiCl_2 is discussed in detail below in order to clarify the contents of Table 5. The experimentally determined and calculated values of V_{33} are listed in columns 2 and 3 of the table, respectively. The chlorine site with the calculated value of V_{33} closest to the experimental V_{33} value was chosen for analysis. Eight NLMOs are listed in column 4 (NLMOs 54−57 are shown in the upper half of Figure 7), since they make contributions to V_{33} larger than |5|% of the total V_{33} value. Columns 5 and 6 indicate the orbital type and occupancy, respectively. The "NLMO composition" in column 7 provides percentage compositions of the NLMOs in terms of atomic orbitals from individual atoms, as printed by the NBO program. The contributions of each atom are further decomposed into percentage contributions from specific atomic orbitals (e.g., 2s, 3d). The Lewis, non-Lewis, and total contributions to V_{33} made by each NLMO are given in columns 8−10, respectively.

NLMOs 36−38 completely consist of core Cl 2p orbitals. The individual Lewis contributions of NLMOs 36−38 to V_{33} are very large; however, because they correspond to a closed 2p shell, their combined contribution to V_{33} amounts to only 0.193 atomic units (au). A filled subshell of AOs should make no net contribution to the EFG tensor because of its spherical symmetry; however, in this case, the nonzero contribution of orbitals 36−38 to V_{33} arises from the deformation of these orbitals by nearby atoms and bonds and core–valence orthogonalization. The small combined contribution of the core Cl NLMOs is seen for both of the other systems as well. NLMOs 54−57, primarily composed of Cl 3s and 3p AOs, contribute 1.362 au to V_{33}, representing a large portion of the total of 1.470 au. NLMOs 54 and 57 make large negative contributions to V_{33} and represent a nonbonding lone pair and Ti−Cl σ bond, respectively. NLMOs 55 and 56 make large positive contributions to V_{33} and represent lone pairs that participate in Ti−Cl π bonding. It is evident that NLMO 56 represents a greater degree of Ti−Cl π bonding than NLMO 55, as indicated by the lower occupancy (1.83 vs 1.92) of its parent NBO and its larger fraction of Ti character (8.7 vs 2.7%). It also makes a smaller contribution to V_{33} than NLMO 55 (3.895 vs 4.377 au).

Bryukhova and co-workers[44,45] have previously hypothesized that increased Ti−Cl π bonding leads to a decrease in the observed $^{35/37}$Cl EFGs. This hypothesis was used to explain the large decrease in C_Q observed when the ^{35}Cl NQR data from $CpTiCl_3$ and Cp_2TiCl_2 were compared. It is interesting to see whether this hypothesis can be confirmed by comparing the NLMO EFG analyses of Cp_2TiCl_2 and $CpTiCl_3$. The NLMO EFG analysis of $CpTiCl_3$ is shown in Table 5, and NLMOs 47−49 and 1 are shown in the bottom half of Figure 7.

Minor negative contributions to V_{33} from core Ti AOs are observed for $CpTiCl_3$, which likely arise because of much shorter Ti−Cl bond lengths than in Cp_2TiCl_2. The majority of V_{33} is seen to once again arise from contributions from the valence Cl AOs and Ti−Cl bonding orbitals, which are described by NLMOs 47−49 and 1. The nonbonding Cl lone-pair orbital, NLMO 47, and one of the π-bonding electron lone pairs, NLMO 48, make contributions to V_{33} that are similar in sign and magnitude to those of their counterparts in Cp_2TiCl_2 (NLMOs 54 and 55, respectively). However, the remaining two Cl electron lone pairs of $CpTiCl_3$ are quite different from those of Cp_2TiCl_2. NLMO 49 is classified as a "lone pair" by the NBO program, but it is evident from its appearance and low occupancy (1.69) that NLMO 49 represents a significant degree of Ti−Cl bonding. The contribution to V_{33} from NLMO 49 is −2.923 au, which is of the same sign and smaller in magnitude than that from the σ-bonding lone pair of Cp_2TiCl_2 (NLMO 57, −4.743 au). NLMO 1 is classified as a bonding orbital and possesses a high occupancy (1.99). The V_{33} contribution by NLMO 1 (1.692 au) is of the same sign as that of the π-bonding lone pair of Cp_2TiCl_2 (NLMO 56); however, the magnitude of the contribution is significantly smaller. The V_{33} contributions from NLMOs 1 and 49 in $CpTiCl_3$ total −1.231 au, which can be compared with the total of −0.848 au from NLMOs 56 and 57 of Cp_2TiCl_2. In summary, it is clear from the visualization of NLMOs 48, 49, and 1 of $CpTiCl_3$ and the much lower parent NBO occupancies for NLMOs 48 and 49 that there is much more π bonding in $CpTiCl_3$ than in Cp_2TiCl_2. The comparison of the NLMOs and EFG tensors in $CpTiCl_3$ and Cp_2TiCl_2 makes clear the fact that the decreased V_{33} contributions from the $CpTiCl_3$ NLMOs arise from increased Ti−Cl π-bonding char-

(78) Autschbach, J. *J. Chem. Phys.* **2007**, *127*, 124106.
(79) Autschbach, J. *J. Chem. Phys.* **2008**, *128*, 164112.
(80) Autschbach, J.; Le Guennic, B. *J. Chem. Educ.* **2007**, *84*, 156–171.
(81) Boshaalaa, A. M. A.; Simpson, S. J.; Autschbach, J.; Zheng, S. *Inorg. Chem.* **2008**, *47*, 9279–9292.

Table 5. Analysis of NLMO Contributions to the EFG Tensors for Cp_2TiCl_2, $CpTiCl_3$, and Cp_2ZrCl_2

	V_{33} (au)						contributions to V_{33} (au)		
compound	exptl[a]	calcd	NLMO no.[b]	orbital type[c]	occ[d]	NLMO composition[e]	Lewis	non-Lewis	total[f]
Cp_2TiCl_2	1.152	1.386	36	core	2.00	100 Cl (100 2p)	79.634	0.020	79.654
			37	core	2.00	100 Cl (100 2p)	52.764	0.013	52.777
			38	core	2.00	100 Cl (100 2p)	−132.225	−0.013	−132.238
						sum of core orbital contributions:	0.173	0.020	0.193
			54	lone pair, nb	1.97	1.2 Ti (24.6 4s, 74 3d), 98.7 Cl (70.5 3s, 29.5 3p)	−2.112	−0.055	−2.167
			55	lone pair, π	1.92	2.7 Ti (99.4 3d), 96.1 Cl (100 3p)	4.577	−0.200	4.377
			56	lone pair, π	1.83	8.7 Ti (99.3 3d), 90.6 Cl (99.3 3p)	4.140	−0.245	3.895
			57	lone pair, σ	1.61	21.1 Ti (10.8 4s, 88.6 3d), 76.5 Cl (28.7 3s, 71.0 3p)	−5.362	0.619	−4.743
						sum of Cl lone-pair/bonding orbital contributions:	1.243	0.119	1.362
			62	Cp lone pair	1.05	17.9 Ti (99.2 3d), 1.9 Cl (28.4 3s, 70.8 3p), 80.1 Cp C	0.018	−0.103	−0.085
						sum of NLMO contributions:	1.434	0.036	1.470
$CpTiCl_3$	0.808	0.789	20	core	2.00	100 Ti (100 3s)	−0.066	0.000	−0.066
			22	core	2.00	100 Ti (100 3p)	−0.041	0.002	−0.039
			26	core	2.00	100 Ti (100 3p)	−0.058	0.003	−0.055
						sum of Ti core orbital contributions:	−0.165	0.005	−0.160
			29	core	2.00	100 Cl (100 2p)	−62.120	−0.001	−62.121
			30	core	2.00	100 Cl (100 2p)	79.956	0.009	79.965
			31	core	2.00	100 Cl (100 2p)	−17.743	0.001	−17.742
						sum of Cl core orbital contributions:	0.093	0.009	0.102
			47	lone pair, nb	1.98	1.0 Ti (9.4 4s, 89.6 3d), 99.0 Cl (68.4 3s, 31.6 3p)	−2.138	−0.045	−2.183
			48	lone pair, π	1.79	9.2 Ti (99.3 3d), 89.2 Cl (100 3p)	4.323	−0.257	4.066
			49	lone pair, σ/π	1.69	13.1 Ti (11.3 4s, 87.7 3d), 84.5 Cl (11.8 3s, 88 3p)	−3.618	0.695	−2.923
			1	bond, σ/α	1.99	13.5 Ti (16.4 4s, 83.1 3d), 86.3 Cl (18.3 3s, 81.5 3p)	1.766	−0.074	1.692
						sum of Cl lone-pair/bonding orbital contributions:	0.333	0.319	0.652
			53	Cp−Ti, π	1.05	79.6 Cp C, 17.5 Ti (97.1 3d), 2.1 Cl (91.5 3p)	−0.010	0.105	0.095
						sum of NLMO contributions:	0.251	0.438	0.689
Cp_2ZrCl_2	0.834	0.895	28	core	2.00	99.5 Zr (99.99 4s)	−0.054	0.000	−0.054
			37	core	2.00	100 Zr (100 4p)	−0.052	0.005	−0.048
			50	core	2.00	100 Cl (100 2p)	77.536	0.018	77.554
			51	core	2.00	100 Cl (100 2p)	56.132	0.016	56.148
			52	core	2.00	100 Cl (100 2p)	−133.574	0.014	−133.560
						sum of Cl core orbital contributions:	0.094	0.048	0.142
			67	lone pair, nb	1.98	1.0 Zr (13.4 5s, 85.5 4d), 98.9 Cl (63.4 3s, 36.6 3p)	−2.677	0.014	−2.663
			68	lone pair, π	1.91	3.9 Zr (98.6 4d), 95.0 Cl (99.9 3p), 0.9 Cp C	4.624	−0.241	4.383
			69	lone pair, π	1.85	7.8 Zr (98.7 4d), 91.7 Cl (1.0 3s, 98.9 3p)	4.074	−0.286	3.788
			70	lone pair, σ	1.70	15.3 Zr (15.1 5s, 84.2 4d), 83.5 Cl (35.5 3s, 64.3 3p)	−5.213	0.553	−4.660
						sum of Cl lone pair/bonding orbital contributions:	0.808	0.040	0.848
						sum of NLMO contributions:	0.796	0.092	0.888

[a] Experimental values of C_Q were converted to V_{33} values. The sign of V_{33} cannot be determined experimentally. [b] Index number assigned by the NBO program. [c] Label assigned by the NBO program: "bond" refers to a bonding orbital, "core" to a nonbonding orbital in the subshell below the valence shell, and "lone pair" to a lone pair localized on Cl. The chlorine lone pairs have also been qualitatively described as nonbonding (nb) or participating in Ti−Cl π or σ bonding. [d] Occupancy of the parent NBO of the NLMO; the analysis data is for the NLMO itself. Occupancies <2 indicate deviation from an ideal Lewis structure. [e] The number before each atom symbol indicates the percentage contribution to the NLMO from AOs of that atom. The contribution from that atom is then broken down by percentage of each orbital type (i.e., s, p, d). [f] Values of V_{33} obtained by summing all of the printed NLMO contributions differ from the calculated V_{33} values because of the exclusion of many small contributions that are not printed.

acter, in agreement with Bryukhova's hypothesis,[44,45] which was based upon the semiempirical Townes−Daily theory.[82]

Finally, the NLMO analysis of Cp_2ZrCl_2 is compared with that of Cp_2TiCl_2 in order to explain the large differences in their C_Q values. The reduced C_Q in Cp_2ZrCl_2 occurs for the following reasons: First, minor negative contributions to V_{33} are seen to arise from NLMO 28 and 37, which comprise core Zr 4s and 4p AOs. Second, the major reduction in C_Q seems to arise from the valence Cl 3s and 3p orbitals [NLMOs 67−70 (Figure 8)], where the contributions to V_{33} are reduced by 0.514 au. This is mainly due to a large increase in the magnitude of the negative contribution (−2.663 au) from the nonbonding Cl electron lone pair, NLMO 67. The nonbonding lone pair has much greater p character in Cp_2ZrCl_2 (36.6%) than in Cp_2TiCl_2 (29.5%), resulting in a more asymmetric distribution of charge and a larger negative contribution to V_{33}.

^{35}Cl SSNMR Spectroscopy and Quantum-Chemical Modeling of Cp_2ZrHCl. Cp_2ZrHCl (Schwartz's reagent) was first synthesized in the 1970s,[83−85] and the utility of the compound as a reagent for hydrogenation, halogenation, and carbon−carbon bond-formation reactions was quickly realized.[86,87] Development of new reactions that utilize this complex continues today.[88−90] There is currently no known single-crystal or powder X-ray diffraction structure of Cp_2ZrHCl. In order to probe the solid-

(82) Townes, C. H.; Dailey, B. P. *J. Chem. Phys.* **1949**, *17*, 782–796.
(83) Wailes, P. C.; Weigold, H.; Bell, A. P. *J. Organomet. Chem.* **1971**, *27*, 373–378.
(84) Wailes, P. C.; Weigold, H. *J. Organomet. Chem.* **1970**, *24*, 405–411.
(85) Kautzner, B.; Wailes, P. C.; Weigold, H. *J. Chem. Soc., Chem. Commun.* **1969**, 1105.
(86) Schwartz, J.; Labinger, J. A. *Angew. Chem., Int. Ed. Engl.* **1976**, *15*, 333–340.
(87) Hart, D. W.; Schwartz, J. *J. Am. Chem. Soc.* **1974**, *96*, 8115–8116.
(88) Spletstoser, J. T.; White, J. M.; Tunoori, A. R.; Georg, G. I. *J. Am. Chem. Soc.* **2007**, *129*, 3408–3419.
(89) Wipf, P.; Nunes, R. L. *Tetrahedron* **2004**, *60*, 1269–1279.
(90) Wipf, P.; Jahn, H. *Tetrahedron* **1996**, *52*, 12853–12910.

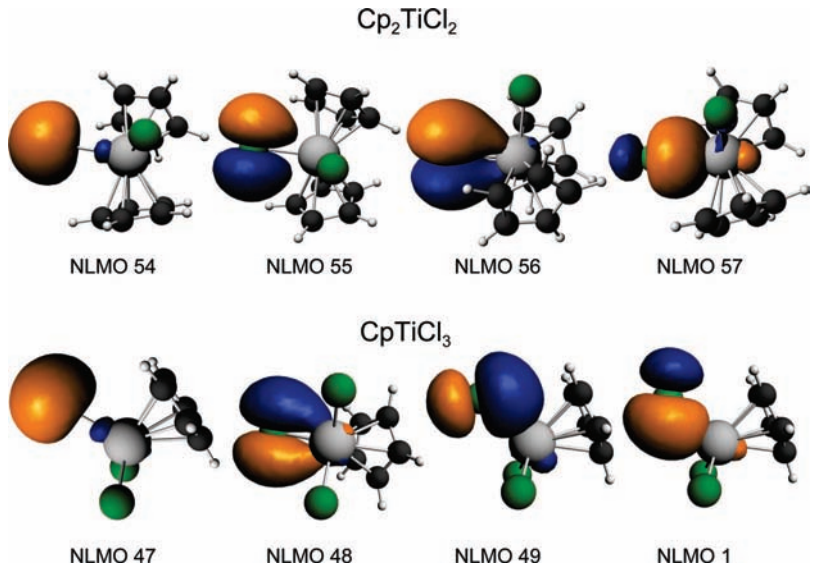

Figure 7. Images of NLMOs that are the main contributors to the observed ^{35}Cl EFGs in (top) Cp_2TiCl_2 and (bottom) $CpTiCl_3$. The contributions of the individual NLMOs to the observed ^{35}Cl EFGs are given in Table 5.

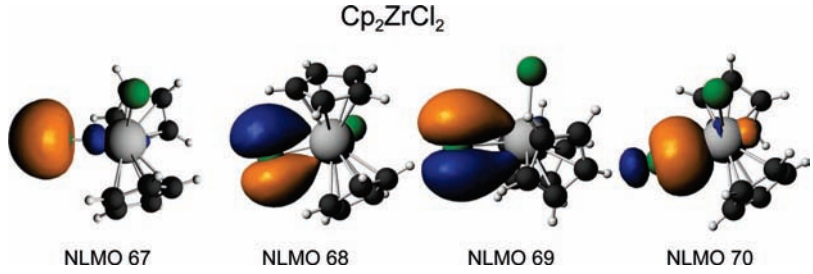

Figure 8. Images of NLMOs that are the main contributors to the observed ^{35}Cl EFGs in Cp_2ZrCl_2.

state structure of this important reagent, the ^{35}Cl SSNMR spectrum was acquired and quantum-chemical calculations on several models were performed using the methodologies discussed above.

The ^{35}Cl SSNMR spectra and analytical simulations for Cp_2ZrHCl are shown in Figure 9. The spectra very closely conform to that of a standard quadrupolar powder pattern, indicating that the powdered sample is crystalline (powder X-ray diffraction also confirms this; see Figure S3 in the Supporting Information) and contains one type of chlorine ligand. The ^{35}Cl NMR spectrum at 9.4 T is best simulated with $C_Q = 19.7$ MHz, $\eta_Q = 0.20$, and $\delta_{iso} = 80$ ppm (Table 1). Simulations of the spectra at 21.1 T utilized $\Omega = 400$ ppm and $\kappa = 0.5$ (Table 6) and nonzero Euler angles [$\alpha = \gamma = 0(30)°$, $\beta = 85(30)°$]. The chlorine CSA is much smaller than those observed for Cp_2ZrCl_2 and $CpTiCl_3$.

Previously acquired IR spectra of Cp_2ZrHCl and Cp_2ZrDCl suggest that the hydride ligands bind in a bridging manner, implying that the complex exists as an oligomer in the solid state.[84,85] The observed ^{35}Cl NMR parameters unequivocally confirm this hypothesis. The value of C_Q is significantly larger than that observed for Cp_2ZrCl_2. The observed value of η_Q is similar to the small values of η_Q observed for the terminal chloride ligands of Cp*$ZrCl_3$ and $(Cp_2ZrCl)_2\mu$-O and distinct from the intermediate to large η_Q values observed for all of the monomeric complexes that possess terminal chloride ligands. This indicates that the complex is a dimer that contains bridging hydride ligands and terminal chloride ligands. The application of ^{1}H decoupling during the acquisition of the subspectra greatly lengthens the time for which echoes can be acquired with the QCPMG sequence. This subsequently improves the signal-to-noise ratio of the spectrum (see the inset of Figure 9 and Figure S4 in the Supporting Information) and indicates the proximity of the hydride and chlorine atoms.

In order to confirm the model derived from experiment, quantum-chemical calculations of ^{35}Cl EFG and CS tensors were performed on a series of model structures. As a starting point for developing our structural models, a search of the Cambridge Structural Database (CSD) for other bis(cyclopentadienyl)zirconium hydride complexes was performed. A single-crystal X-ray structure was found for methylbis(cyclopentadienyl)zirconium hydride (Cp_2ZrHMe),[91] which exists as a dimer in the solid state. In view of the similarity of the molecular structures of Cp_2ZrCl_2 and $Cp_2ZrMeCl$, Cp_2ZrHMe seemed to be a reasonable starting point for modeling the solid-state structure of Cp_2ZrHCl. Monomeric bis(cyclopentadienyl)zirconium chloride hydride and dihydride structures were also located, but all of these complexes contained bulky, substituted Cp ligands, which have a strong influence on the structure and chemistry in general.[92,93]

Two models were constructed from the crystal structure of Cp_2ZrHMe (Figure 10). The positions of the Zr, hydride, and

(91) Harlan, C. J.; Bott, S. G.; Barron, A. R. *J. Chem. Soc., Dalton Trans.* **1997**, 637–641.
(92) Bradley, C. A.; Lobkovsky, E.; Keresztes, I.; Chirik, P. J. *J. Am. Chem. Soc.* **2006**, *128*, 6454–6467.
(93) Pool, J. A.; Bradley, C. A.; Chirik, P. J. *Organometallics* **2002**, *21*, 1271–1277.

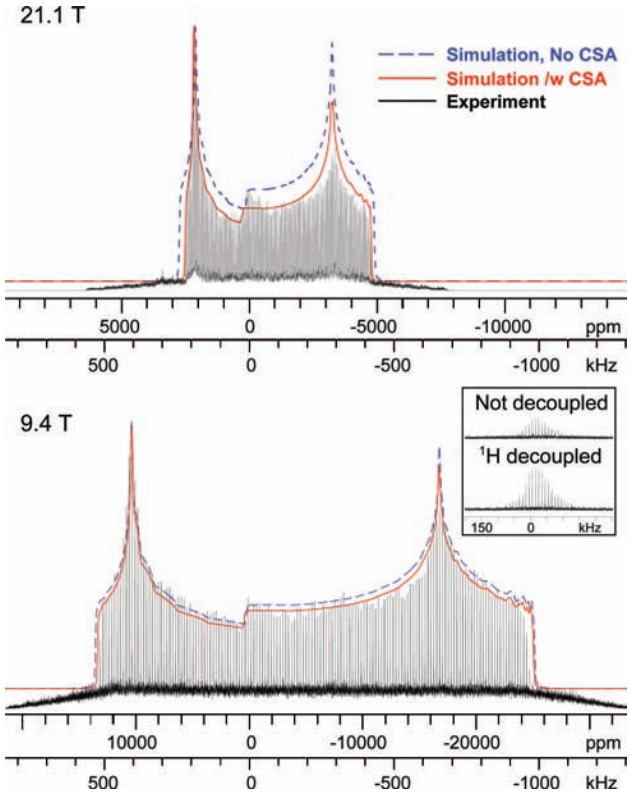

Figure 9. ^{35}Cl SSNMR spectra of Cp_2ZrHCl acquired at 9.4 and 21.1 T and analytical simulations of the spectra. Simulations with (solid red traces) and without (dashed blue traces) the effects of CSA are shown. The effects of ^{1}H decoupling on an individual subspectrum from 9.4 T are shown in the inset. The application of ^{1}H decoupling greatly increases the number of echoes that may be acquired and leads to a dramatic increase in the signal-to-noise ratio.

Table 6. Observed and Calculated ^{35}Cl NMR Parameters for Cp_2ZrHCl[a]

compound	method/basis set	C_Q (MHz)	η_Q	δ_{iso} (ppm)	Ω (ppm)	κ
Cp_2ZrHCl	experimental	19.7	0.2	80	400(250)	0.5(5)
model 1	RHF/aug-cc-pVDZ	−20.9	0.1	−40	318	0.9
	B3LYP/aug-cc-pVDZ	−23.1	0.15	124	485	0.7
model 2	RHF/aug-cc-pVDZ	−18.9	0.12	6	351	0.9
	B3LYP/aug-cc-pVDZ	−21.1	0.18	154	476	0.8
model 3	RHF/aug-cc-pVDZ	11.5	0.94	224	793	−0.3
	B3LYP/aug-cc-pVDZ	13.4	0.55	482	1074	−0.2

[a] See the footnotes of Tables 1 and 3 for definitions of the parameters.

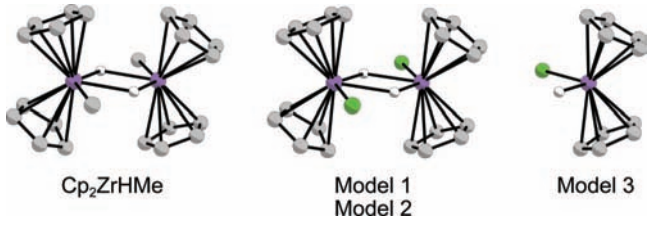

Figure 10. Structures of Cp_2ZrHMe and models of the solid-state structure of Cp_2ZrHCl. Cartesian coordinates of the atomic positions for each model are given in Table S4 in the Supporting Information.

Cp carbon atoms were not altered in either model. In model 1, the methyl ligand was replaced with a chloride ligand. The positions of the Cl and Cp H atoms were geometry optimized. Optimized Cl−Zr bond lengths of 2.61 Å (RHF) and 2.56 Å (B3LYP) were obtained, and calculations with both methods resulted in an angular displacement of the Cl ligand by ∼2° from the position of the methyl carbon (Cartesian coordinates for all of the models are given in Table S4 in the Supporting Information). Calculations of ^{35}Cl NMR parameters from model 1 yielded reasonable agreement with the experimental parameters (Table 6). Model 2 was identical to model 1, except that the Zr−Cl bond lengths were set to a more reasonable distance of 2.46 Å, based on the terminal Zr−Cl bond lengths observed in other zirconium complexes. The calculated EFG tensor parameters for model 2 were in better agreement with the experimental values than those of model 1. The success of the calculations on models 1 and 2 at reproducing the experimental NMR parameters suggest that they are accurate representations of the molecular structure.

Powder X-ray diffraction results also support the proposed structural model of Cp_2ZrHCl. The observed powder X-ray diffraction pattern of Cp_2ZrHCl bears a striking resemblance to that predicted from the single-crystal X-ray structure of Cp_2ZrHMe (Figure S3 in the Supporting Information). If the methyl group in the crystal structure of Cp_2ZrHMe is removed and a Cl atom placed at the methyl carbon position, the powder X-ray diffraction pattern predicted from this "rough" crystal structure of Cp_2ZrHCl is seen to provide an extremely close match with the experimental diffraction pattern. While a full Rietveld refinement of Cp_2ZrHCl was beyond the scope of this study, the diffraction results suggest that the proposed dimer structure of Cp_2ZrHCl is correct and that it crystallizes in the same space group as Cp_2ZrHMe with very similar unit cell parameters.

Finally, to demonstrate that the ^{35}Cl NMR parameters are distinct for monomeric and dimeric species, a third model was constructed from the crystal structure of the monomeric complex $Cp_2ZrMeCl$ (Figure 10). The methyl ligand was replaced with a hydride, and the hydride and chloride positions were optimized. Calculations on model 3 result in values of C_Q and η_Q that show very poor agreement with experimental values. Furthermore, the B3LYP values of δ_{iso} for models 1 and 2 are in good agreement with the experimental parameters, while calculated values for model 3 are not. The calculated values of Ω and κ from models 1 and 2 are quite distinct from those of model 3 as well, demonstrating the potential of CS tensor parameters for distinguishing between monomeric and dimeric structures.

Conclusions

Extremely broad ^{35}Cl NMR spectra of early-transition-metal organometallic complexes can be acquired with the QCPMG sequence in experimental times of 2−28 h at a moderate magnetic field of 9.4 T. The acquisition of ^{35}Cl spectra at 21.1 T results in an order of magnitude reduction of the experimental times compared with those at 9.4 T. It was possible to acquire high-quality ^{35}Cl spectra of Cp_2ZrCl_2 and $CpTiCl_3$ in less than 13 min at 21.1 T as a result of increases in the signal-to-noise ratios and reductions in the breadths of the ^{35}Cl powder patterns. This suggests that it is possible to utilize ^{35}Cl NMR spectroscopy to probe surface-supported organometallic complexes despite the low loading levels (∼5 wt % catalyst or less). The ^{35}Cl NMR parameters act as sensitive probes of molecular structure because of their dependence upon the number and types of ligands coordinated to the metal center(s) to which the Cl atoms are bound. Chlorine CSA is quite large and may be observed in high-field NMR spectra. Quantum-chemical calculations can accurately reproduce the experimentally observed NMR pa-

rameters. In particular, NLMO EFG analyses should shed much light on the relationships between EFG tensors and molecular symmetry and bonding. NMR spectra, powder X-ray diffraction data, and theoretical methods demonstrate that Cp_2ZrHCl exists as a dimer in the solid state and possesses a structure similar to that of Cp_2ZrHMe. The tandem of ^{35}Cl NMR spectroscopy and quantum-chemical calculations will ultimately allow one to examine the molecular structures of surface-supported organometallics.

While this work has focused on the ^{35}Cl NMR spectroscopy of early-transition-metal metallocenes, it is clear that the methods described herein can easily be extended to characterization of countless chlorine-containing main-group and transition-metal coordination compounds. Lucken[38] has summarized the values of $\nu_Q(^{35}Cl)$ obtained from NQR spectra of chloride complexes of B, Al, Ga, Si, Sn, Sb, and Bi, and the corresponding values of $C_Q(^{35}Cl)$ for these complexes range from ~9 MHz (Al complexes) to 40 MHz (Si, Sn, and Sb complexes). The values of $\nu_Q(^{35}Cl)$ observed for late-transition-metal complexes (e.g., Re, Os, Pt) indicate that rapid acquisition of ^{35}Cl SSNMR spectra of these complexes is also feasible. The combination of high magnetic fields (e.g., 21.1 T) and new NMR techniques designed to increase excitation bandwidths[94,95] should permit comprehensive structural characterization of inorganic species in a variety of solid phases by ^{35}Cl SSNMR, especially those for which single-crystal X-ray data is unavailable.

Experimental Section

Materials. Samples of Cp_2TiCl_2, $CpTiCl_3$, Cp_2ZrCl_2, $Cp^*_2ZrCl_2$, Cp_2ZrHCl, and Cp^*ZrCl_3 were obtained from Strem Chemicals. Samples of Cp_2HfCl_2 and $CpZrCl_3$ were obtained from Sigma-Aldrich. All of the commercially obtained samples were used without further purification. $(Cp_2ZrCl)_2\mu$-O was synthesized according to published procedures.[84] $Cp_2ZrMeCl$ was obtained from the synthesized sample of $(Cp_2ZrCl)_2\mu$-O by the previously published method. Details on the synthesis of both compounds are given in the Supporting Information. The bulk purities of $(Cp_2ZrCl)_2\mu$-O and $Cp_2ZrMeCl$ were confirmed by powder X-ray diffraction (Figure S5 in the Supporting Information). All of the samples were handled in a nitrogen atmosphere glovebox, except for Cp_2HfCl_2, $CpZrCl_3$, and $(Cp_2ZrCl)_2\mu$-O, which were handled in an argon-filled glovebag.

^{35}Cl SSNMR Spectra. Solid-state ^{35}Cl NMR spectra were acquired on a wide-bore Oxford 9.4 T magnet [$\nu_0(^1H) = 400$ MHz, $\nu_0(^{35}Cl) = 39.16$ MHz] with a Varian Infinity Plus console running Spinsight software. High-field ^{35}Cl NMR spectra were acquired on a standard-bore 21.15 T magnet [$\nu_0(^1H) = 900$ MHz, $\nu_0(^{35}Cl) = 88.2$ MHz] with a Bruker Avance II console running TopSpin software. ^{35}Cl NMR experiments at 9.4 T were acquired with a Varian/Chemagnetics 5 mm HX static probe. Experiments at 21.1 T were conducted on a home-built single-channel 5 mm probe. Each sample was finely ground, packed into a filed 5 mm glass NMR tube, capped, and sealed with Parafilm. ^{35}Cl chemical shifts were reported with respect to an infinitely dilute solution of NaCl(aq) ($\delta_{iso} = 0.0$ ppm) by the use of a secondary standard of NaCl(s) for which $\delta_{iso} = -45.37$ ppm.[33] Pulse calibrations were performed on a saturated solution of NaCl(aq), and central-transition selective $\pi/2$ pulse widths were calculated by scaling the solution pulse widths by a factor of $1/2$, i.e. $(I + 1/2)^{-1}$. The QCPMG pulse sequence of the form $\{\pi/2 - [\tau - \pi - \tau - \text{acquire}]_N\}$ was used for the acquisition of ^{35}Cl NMR spectra.[56] The number of refocusing π pulses varied from 20 to 162 depending upon the sample. A detailed list of experimental parameters can be found in Tables S5 and S6 in the Supporting Information. All of the spectra were processed on a personal computer with the NUTS program from Acorn Software. The FIDs of subspectra were left-shifted where necessary, apodized using a Gaussian function of less than 100 Hz, digitally filtered to remove frequencies outside of 200 kHz, Fourier transformed, and magnitude-calculated. The individual subspectra were then coadded to form the total pattern. Curved baselines are visible in some spectra and are apparent when relatively low signal-to-noise subspectra are coadded to generate total NMR spectra. The curved baselines did not affect the positions of discontinuities and hence did not affect the NMR parameters extracted from the simulations. Analytical simulations of the ^{35}Cl SSNMR spectra were performed using the WSolids computer program.[96]

X-ray Diffraction Studies. Single crystals of $CpTiCl_3$ were recrystallized from CH_2Cl_2. Crystals were coated in Paratone oil to prevent the adsoprtion of water. Single-crystal diffraction experiments were performed on a Siemens SMART System CCD diffractometer at room temperature. The data were processed using the SAINT+ software package,[106] and an absorption correction was applied to the data using SADABS. The structure was solved by direct methods and refined by full-matrix least-squares against F^2 using the SHELXTL software package.[107,108] Experimental parameters are provided in Table S1 in the Supporting Information. Samples for powder X-ray diffraction were placed into 1.0 mm glass capillary tubes and flame-sealed. Powder X-ray diffraction patterns were collected using a Bruker AXS HI-STAR system using a General Area Detector Diffractions system. The X-ray source produced Cu Kα radiation ($\lambda = 1.540598$ Å), and an area detector using a 2θ range of 4.0−65.0° was employed. Powder X-ray diffraction patterns were simulated with the Powder Cell software package.[109]

Theoretical Methods

CS and EFG Tensor Calculations. Calculations of CS and EFG tensors were performed using Gaussian 03.[74] Molecular coordinates were input from structures determined by single-crystal X-ray diffraction experiments, and proton positions were geometry-optimized. Calculations were carried out using RHF and hybrid DFT employing the B3LYP hybrid functional.[97] The Dunning-type basis sets indicated in the text and Supporting Information were utilized for Cl.[98,99] The 6-311G** basis set was employed for Ti, C, H, and O. The Zr-5F3 basis set of Huzinaga[100] was employed for Zr. The LANL2DZ electron core potential (ECP) basis set of Hay and Wadt[101,102] was employed for Hf in calculations on Cp_2HfCl_2. CS tensors were calculated using the gauge-including atomic orbitals (GIAO) method.[103,104] HCl was chosen as a chemical shielding standard, and calculated chemical shieldings (σ) were converted to chemical shifts as described in footnote[d] of Table 4.[105]

NLMO EFG Analyses. The NLMO EFG analyses were performed using the Amsterdam Density Functional (ADF) program[75−77] and the NBO 5.0 code.[111–113] The ADF calculations utilized the B3LYP functional with all-electron doubly polarized

(94) Bhattacharyya, R.; Frydman, L. *J. Chem. Phys.* **2007**, *127*, 194503.
(95) O'Dell, L. A.; Schurko, R. W. *Chem. Phys. Lett.* **2008**, *464*, 97–102.
(96) Eichele, K.; Wasylishen, R. E. *WSolids: Solid-State NMR Spectrum Simulation Package*; 2001.
(97) Lee, C.; Yang, W.; Parr, R. G. *Phys. Rev. B* **1988**, *37*, 785–789.
(98) Woon, D. E.; Dunning, T. H. *J. Chem. Phys.* **1995**, *103*, 4572–4585.
(99) Dunning, T. H. *J. Chem. Phys.* **1989**, *90*, 1007–1023.
(100) Huzinaga, S. *Gaussian Basis Sets for Molecular Calculations*; Elsevier: New York, 1984.
(101) Hay, P. J.; Wadt, W. R. *J. Chem. Phys.* **1985**, *82*, 270–283.
(102) Hay, P. J.; Wadt, W. R. *J. Chem. Phys.* **1985**, *82*, 299–310.
(103) Ditchfield, R. *Mol. Phys.* **1974**, *27*, 789–807.
(104) Wolinski, K.; Hinton, J. F.; Pulay, P. *J. Am. Chem. Soc.* **1990**, *112*, 8251–8260.
(105) Gee, M.; Wasylishen, R. E.; Laaksonen, A. *J. Phys. Chem. A* **1999**, *103*, 10805–10812.

triple-ζ basis sets on all atoms. The theoretical basis of the NLMO EFG analysis is described in the next paragraph.

For nonrelativistic computations of EFG tensor components[110] and their subsequent analysis in terms of localized or delocalized orbitals, consider V_{uv}, the second derivative of the electric potential V:

$$V_{uv} = \frac{\partial^2 V}{\partial u\, \partial v} \qquad u, v \in \{x, y, z\} \tag{2}$$

where $\mathbf{r} = (x, y, z)$ is the position vector of a point in the Cartesian laboratory coordinate frame. This tensor element is evaluated at the position $\mathbf{R}_A$ of nucleus A. There is an electronic contribution V_{uv}^{el}, given by

$$V_{uv}^{el}(\mathbf{R}_A) = \int d^3r\, \rho(\mathbf{r}) \hat{V}_{uv}^{el}(\mathbf{r}, \mathbf{R}_A) \tag{3}$$

in which $\rho(\mathbf{r})$ is the electron density and the electronic EFG operator $\hat{V}_{uv}^{el}$ is defined as

$$\hat{V}_{uv}^{el}(\mathbf{r}, \mathbf{R}_A) = -\frac{3(\mathbf{r} - \mathbf{R}_A)_u(\mathbf{r} - \mathbf{R}_A)_v - \delta_{uv}|\mathbf{r} - \mathbf{R}_A|^2}{|\mathbf{r} - \mathbf{R}_A|^5} \tag{4}$$

where δ_{uv} is the Kronecker delta. The nuclear contribution V_{uv}^{nuc} is given by

$$V_{uv}^{nuc}(\mathbf{R}_A) = \sum_{B \neq A} Z_B \frac{3(\mathbf{R}_B - \mathbf{R}_A)_u(\mathbf{R}_B - \mathbf{R}_A)_v - \delta_{uv}|\mathbf{R}_B - \mathbf{R}_A|^2}{|\mathbf{R}_B - \mathbf{R}_A|^5} \tag{5}$$

where Z_B is the charge of nucleus B. Because of the opposite signs of the electronic and nuclear contributions, there are numerous cancelations between these terms, which is undesirable for an MO analysis. For example, the core electron density of a neighboring atom cancels part of the nuclear charge contribution from this atom, reducing Z_B to an effective nuclear charge. Moreover, for an MO analysis, it is preferable to define the nuclear contribution as an integral over space just like the electronic term. It is therefore desirable to compute the electronic and nuclear terms together. Thus, a nuclear operator $\hat{V}_{uv}^{nuc}$ is defined as

$$\hat{V}_{uv}^{nuc}(\mathbf{r}, \mathbf{R}_A) = \frac{1}{N} V_{uv}^{nuc}(\mathbf{R}_A) \tag{6}$$

where N is the number of electrons in the molecule. The total EFG tensor element uv is then given by the expression

$$V_{uv}(\mathbf{R}_A) = \int d^3r\, \rho(\mathbf{r}) \left[\hat{V}_{uv}^{el}(\mathbf{r}, \mathbf{R}_A) + \hat{V}_{uv}^{nuc}(\mathbf{r}, \mathbf{R}_A)\right] \tag{7}$$

The electron density $\rho(\mathbf{r})$ is now simply split up into contributions from various sets of orbitals. We chose to use sets of NLMOs (ϕ_j) with occupations (n_j) of 2, as provided by the NBO 5.0 code, meaning that the NLMO EFG analysis is based on using

$$\rho(\mathbf{r}) = \sum_j n_j \phi_j^* \phi_j \tag{8}$$

in eq 7. This partitioning is formally exact, i.e., no approximations beyond use of the density functional and basis set are made in the analysis step.

Acknowledgment. R.W.S. thanks the Natural Science and Engineering Research Council (NSERC, Canada) for research funding and also acknowledges the Canadian Foundation for Innovation (CFI), the Ontario Innovation Trust (OIT), and the University of Windsor for funding the solid-state NMR facility. R.W.S. also thanks the Ontario Ministry of Research and Innovation for an Early Researcher Award. A.J.R. thanks the Ontario Ministry of Education and Training and NSERC for graduate scholarships. J.A. and S.Z. acknowledge financial support from the National Science Foundation (CHE-0447321). Experiments at 21.1 T were conducted at the Canadian National Ultrahigh-field NMR Facility for Solids (www.nmr900.ca). Dr. Victor Terskikh and Dr. Shane Pawsey are thanked for their assistance with all of the experiments at 21.1 T. Mr. Jamie Bennett (NRC, Ottawa) is thanked for construction of the static 5 mm probe used for experiments at 21.1 T.

Supporting Information Available: Complete refs 74 and 75, NMR experiment parameters for each compound, additional figures, tables with all of the Gaussian 03 calculation results, Cartesian coordinates of EFG tensors in molecular frames, a CIF file for $CpTiCl_3$, and Cartesian coordinates of models of Cp_2ZrHCl. This material is available free of charge via the Internet at http://pubs.acs.org.

JA808390A

(106) *SAINT+*, version 6.45; Bruker AXS Inc.: Madison, WI, 2003.
(107) Sheldrick, G. M. *Acta Crystallogr., Sect. A: Found. Crystallogr.* **2008**, *64*, 112–122.
(108) Sheldrick, G. M. *SHELXTL*, version 6.10; Bruker AXS Inc.: Madison, WI, 2000.
(109) Kraus, W.; Nolze, G. *PowderCell for Windows*; Federal Institute for Materials Research and Testing: Berlin, 2000.
(110) For a brief discussion of sign conventions of EFG tensors, please see ref 61.
(111) Bohmann, J. A.; Weinhold, F.; Farrar, T. C. *J. Chem. Phys.* **1997**, *104*, 1173–1184.
(112) Glendening, E. D.; Badenhoop, J. K; Reed, A. E.; Carpenter, J. E.; Bohmann, J. A.; Morales, C. M.; Weinhold, F. *NBO 5.0*; Theoretical Chemistry Institute, University of Wisconsin: Madison, WI, 2001; http://www.chem.wisc.edu/~nbo5 (accessed Feb 10, 2009).
(113) Weinhold, F. In *Encyclopedia of Computational Chemistry*; von Ragué Schleyer, P., Ed.; John Wiley & Sons: Chichester, U. K., 1998; pp 1792–1811.